The DOI for this manuscript is doi: 10.1175/MWR-D-18-0400.1

The Mechanism and Predictability of an Elevated Convection Initiation Event in a Weak-Lifting Environment in Central Eastern China

Murong Zhang[1], Zhiyong Meng[1*], Yipeng Huang[2], and Dongyong Wang[3]

[1]*Laboratory for Climate and Ocean-Atmosphere Studies, Department of Atmospheric and Oceanic Sciences, School of Physics, Peking University, Beijing, China*

[2]*Laboratory of Straits Meteorology, Xiamen Meteorological Bureau, Xiamen, China*

[3]*Anhui Meteorological Bureau, Hefei, China*

23 February 2019

Monthly Weather Review, Minor revision

[*]*Corresponding author address:* Dr. Zhiyong Meng, Laboratory for Climate and Ocean–Atmosphere Studies, Department of Atmospheric and Oceanic Sciences, School of Physics, Peking University, Beijing, China.

E-mail: zymeng@pku.edu.cn

Abstract

An elevated convection initiation (CI) of a quasi-linear mesoscale convective system (MCS) that occurred in a weak-lifting environment in the early morning on 23 June 2016 in central eastern China was investigated using observational analysis and convection-permitting numerical simulations. This MCS gradually developed into a surface-based MCS and eventually produced a strong supercell that spawned an EF4 tornado in Yancheng City of Jiangsu Province and killed 98 people. This elevated MCS was initiated ahead of a surface front without identifiable boundaries at the surface. An elevated moist absolutely unstable layer (MAUL) was found to be conducive to the CI. The MAUL provided negligible convective inhibition and contributed to CI without strong lifting mechanisms. Numerical simulation results showed that the formation of the elevated MAUL was mainly attributed to adiabatic cooling by weak vertical ascent and sufficient horizontal moisture transport near the terminus of a low-level jet. The weak vertical ascent before the CI was sloping and was likely to be relevant to the layer-lifting process associated the realization of potential instability. The results showed that the MAUL in this weak-lifting environment was characterized by a shallower depth, a weaker lapse rate and a longer sustaining period than the conditions in a strong-lifting environment. The predictability of this elevated CI case was examined using a 10-member ensemble forecast. A total of 80% of the ensemble members captured the CI. Rather than a difference in lifting, whether having an elevated MAUL or not was the major difference between CI and non-CI members in the present case.

1. Introduction

Nocturnal mesoscale convective systems (MCSs) frequently occur in many places in the world such as the central U.S. (e.g., Maddox 1980; Carbone et al. 2002; Parker 2008) and central eastern China (e.g., Zheng et al. 2013). These systems produce a considerable portion of the warm-season precipitation (e.g., Wallace 1975; Bentley and Mote 1998; Yu et al. 2007; Chen et al. 2010) and pose a great threat to public safety and property, with hailstorms, flooding and even tornadoes occurring (e.g., Wilson et al. 2018; Trier et al. 2006; Kis and Straka 2010). Nocturnal MCSs are often associated with elevated convection initiation (CI) (e.g., Colman 1990; Weckwerth et al. 2004; Geerts et al. 2017; Reif and Bluestein 2017), where the source of the convective updraft originates above the stable nocturnal planetary boundary layer (PBL). Unlike surface-based CI, elevated CI often occurs without identifiable surface boundaries (e.g., gust fronts and drylines) as precursors (Wilson and Roberts 2006), presenting a great challenge in the forecasting of CI and subsequent MCSs (Davis et al. 2003).

Elevated CI mechanisms have been widely discussed in previous studies. Wilson and Roberts (2006) showed that midlevel convergence and conditional instability were important in initiating nocturnal storms during IHOP_2002 (Weckwerth et al. 2004). Other studies revealed that gravity waves and bores in stable environments are also favorable lifting mechanisms for elevated CI (e.g., Marsham et al 2011; Wilson et al. 2018). Elevated CI, which produces a considerable portion of nocturnal CI (Reif and

60 Bluestein 2017), can occur in an environment with weak but persistent mesoscale ascent
61 without obvious small-scale lifting mechanisms (Trier et al. 2017).

62 Elevated CI in a weak-lifting environment is sometimes characterized by low-level
63 moist absolute unstable layers (MAULs; Bryan and Fritsch 2000), which are saturated
64 layers with lapse rates greater than moist adiabatic rates (i.e., equivalent potential
65 temperature (θ_e) decreasing with height). A MAUL can support elevated CI in the
66 absence of strong vertical motion since all parcels in the MAUL have negligible
67 convective inhibition (CIN) and are unstable in response to slight vertical displacement.
68 Based on observations from the Plains Elevated Convection At Night (PECAN) 2015
69 field campaign (Geerts et al. 2017), recent studies have qualitatively shown that the
70 formation of a MAUL associated with elevated CI may be attributed to a nocturnal low-
71 level jet (LLJ; Gebauer et al. 2018; Shapiro et al. 2018), weak but persistent vertical
72 motion (Trier et al. 2017), and warm advection (e.g., Reif and Bluestein 2017; Wilson
73 et al. 2018). However, the thermodynamic field evolutions associated with the
74 development of elevated MAULs before CI and their quantitative contributions to the
75 formation of MAULs have been less studied. In addition, although the characteristics
76 of MAULs in a strong-lifting environment have been studied in deep convection, such
77 as those in typhoon eyewalls (Barnes 2008) and squall lines (Bryan 2005), the temporal
78 and spatial scales of a MAUL in a weak-lifting environment have rarely been addressed
79 in the literature.

80 The predictability of elevated CI in a weak-lifting environment is also an important

81 issue considering the rather limited prediction capability of state-of-the-art convection-
82 permitting numerical models (Stelten and Gallus 2017). By assimilating *in situ* and
83 radar observations for a nocturnal CI event, Degelia et al. (2018) noted that nocturnal
84 CI forecast accuracy is closely related to the mesoscale preconvective environment.
85 The elevated MAUL in the preconvective environment has been observed as a common
86 feature that promotes elevated CI in the absence of strong lifting mechanisms (e.g.,
87 Trier et al. 2017). However, whether the elevated MAUL can ensure CI in a weak-lifting
88 environment remains unknown. The CI predictability and its relationship with the
89 MAUL in this scenario need to be further investigated.

90 The present work investigates the elevated CI of a linear MCS in central eastern
91 China, where there is the highest recorded rate of squall line incidents in the whole
92 country (Meng et al. 2013; Huang et al. 2017; He et al. 2017). The MCS was initiated
93 at ~0530 LST (LST=UTC+8) 23 June 2016 above a nocturnal stable boundary layer in
94 a weak-lifting environment near the terminus of a LLJ far from the surface front. This
95 linear MCS gradually developed into a surface-based MCS in the daytime and
96 eventually generated an EF4 tornado that killed 98 people, which was the deadliest
97 tornado in the past 41 years in China (Meng et al. 2018). In the current study, analyses
98 were performed based on both observations and convection-permitting simulations to
99 understand the CI, the key factors for the development of an elevated MAUL and the
100 characteristics of the MAUL in this weak-lifting environment. The CI predictability in
101 this scenario and its relationship with the MAUL were also addressed. Section 2

introduces data and methods used in this study. An overview of the CI environment and the evolution of the elevated linear MCS are described in Section 3. Section 4 presents the model configurations, the simulated CI, and the formation mechanisms and characteristics of the MAUL in the weak-lifting environment. The CI predictability in this case and its relationship with the MAUL are also examined using ensemble forecasting. The conclusions of this study are given in Section 5.

2. Data and methods

The data used in this work included radar data, satellite images, high-resolution analysis (HRES) from European Centre for Medium-Range Weather Forecasts (ECMWF), surface observations, and conventional radiosonde observations. Mosaics of composite radar reflectivity were operationally created every 6 min during this event by the China Meteorological Administration (CMA) based on a network of Chinese next-generation weather radars. The Fuyang S-band Doppler radar, which is similar to the Weather Surveillance Radar 1988 Doppler (WSR-88D) (Zhu and Zhu 2004), is located in Anhui Province (locations of the radar and province are denoted in Fig. 1a). Composite true-color images from the Advanced Himawari Imager (AHI) onboard Himawari-8, the new-generation geostationary satellite operated by the Meteorological Satellite Center of the Japan Meteorological Agency, were available every 10 min with a resolution of 1 km at nadir. The HRES analysis from ECMWF (detailed information is available online at https://www.ecmwf.int/en/forecasts/datasets/set-i) is gridded at

123 0.125 º × 0.125º with a 6-h time interval and was used for synoptic analysis and initial
124 and lateral boundary conditions for numerical simulations. 10-min surface observations
125 of automatic weather stations in Anhui province from Anhui Meteorological Bureau
126 and the rawinsonde observation at Fuyang (location denoted in Fig. 2d) from CMA
127 were also used to analyze the CI environment.
128
129 **3. Case overview and observational analysis**
130 A linear MCS occurred in Anhui Province in central eastern China in the early
131 morning on 23 June 2016 under the influence of a LLJ ahead of a surface front (Fig. 1).
132 At 0000 UTC 23 June 2016, this southeast–northwest-oriented linear MCS was located
133 in the warm sector approximately 250 km to the south of the northeast–southwest-
134 oriented surface front (Fig. 1). The synoptic-scale surface front was associated with an
135 ~1000-km-long quasi-linear rainband to the northwest of the target MCS (Fig. 1a). The
136 MCS occurred near the terminus of an 850-hPa strong southwesterly jet[1] without an
137 obvious trough at 500 hPa (Fig. 1b).
138 Observations of the Fuyang radar revealed the detailed initiation of the linear MCS.
139 Several convective cells were initiated (Fig. 2a) in the early morning at 2131 UTC 22
140 June (0531 LST; LST=UTC+8) in the northwest of Anhui Province. These cells then
141 gradually merged into an organized linear MCS and intensified as they moved

[1] 10 m s^{-1} is taken as the threshold for jet region in the present study following Whiteman et al. (1997) and Du et al. (2014)

142 northeastward in the subsequent three hours (Fig. 2b–e). At 0148 UTC 23 June (Fig.
143 2f), the linear MCS moved into Jiangsu Province, gradually developed into a surface-
144 based MCS and eventually spawned a strong supercell at 0600 UTC 23 June at its
145 southern end, which led to a severe tornado (EF4) in Jiangsu Province (Meng et al.
146 2018 in their Fig. 3 and Fig. 8).

147 The composite true-color satellite images from Himawari-8 also successfully
148 captured the CI. Unlike common daytime CI in which cumulonimbus clouds often
149 explosively develop from shallow cumulus or less cloudy conditions, the sky was
150 overcast with stratiform clouds at 2100 UTC 22 June (Fig. 3a) before the CI, which was
151 likely a result of saturation due to layer lifting. At 2110 UTC 22 June, cumuliform
152 protuberances embedded in the stratiform cloud appeared in a similar manner as the
153 appearance of castellanus (Fig 3b), which was possibly associated with elevated
154 convection (Corfidi et al. 2008). These protuberances gradually developed into cumulus
155 cloud cells organized in a northwest–southeast-oriented line (Fig. 3c) and eventually
156 generated deep convection at 2130 UTC 22 June (Fig. 3d and Fig. 2a).

157 Both the surface observations and sounding profiles near the CI location suggested
158 that the initiation of the linear MCS was likely elevated. In the warm sector to the south
159 of the surface front, the near-surface environment was characterized by weak
160 southeasterly wind (~2 m s^{-1}) and relatively uniform temperature and humidity fields
161 (Fig. 4a–d), which indicated the absence of identifiable surface boundaries.
162 Observational evidences of gravity wave aiding CI in the current case were lacking. No

163 obvious wave-like surface pressure patterns (Fig. 4a–d) were found near CI locations.
164 The surface pressure oscillations at stations near CI were also very weak (Fig. 4e)
165 compared with typical mesoscale gravity waves (e.g., Koch and O'Handley 1997, the
166 red curve in Fig. 4e). No alternating bands of radial velocity from Fuyang radar were
167 found either at all elevation angles during 2100–2200 UTC 22 June (figures not shown).
168 The Fuyang radiosonde (location denoted in Fig. 2d) released at 0000 UTC 23 June
169 (Fig. 5) could represent the CI environment even though the CI occurred 150 min
170 previously since the radiosonde was located upstream of the convective line and was
171 not contaminated by convections. There was a temperature inversion near the surface
172 that was likely due to the radiative cooling at night (Fig. 5a). This inversion resulted in
173 a surface-based CIN of 50 J kg^{-1}, and the parcel had to be lifted by 1284 m to reach
174 its LFC. However, the elevated moist layer located between 850 hPa and 600 hPa
175 reduced the CIN for parcels lifted above the stable boundary layer. A parcel lifted from
176 850 hPa had a CIN of 11 J kg^{-1} and a CAPE of 1417 J kg^{-1}, which represented a
177 favorable environment for elevated CI (Fig. 5a). The hodograph (Fig. 5b) revealed the
178 LLJ at 850 hPa and the strong vertical wind shear below 3 km with the 0–3 km AGL
179 layer bulk wind difference of 9.69 m s^{-1}, which were beneficial for the development
180 of an MCS.
181
182 **4. Numerical simulation results**
183

184 *a. Model configurations*

185 To understand the CI and its environmental conditions, a 24-h convection-
186 permitting numerical simulation was conducted from 1200 UTC 22 June to 1200 UTC
187 23 June 2016 using version 3.7.1 of the WRF-ARW model (Skamarock et al. 2008).
188 Initial and lateral boundary conditions were obtained from HRES analysis (gridded at
189 0.125 º × 0.125º), and the lateral boundary conditions were updated every 6 hours.
190 Three two-way nested domains (Fig. 6) with 27-, 9- and 3-km horizontal grid spacing
191 and 41 vertical levels were used. The Single-Moment 6-Class Microphysics scheme
192 (WSM6; Hong and Lim 2006), the Yonsei State University PBL scheme (YSU; Hong
193 et al. 2006), and the rapid radiative transfer model (RRTM) longwave radiation scheme
194 (Mlawer et al. 1997) were used for all three domains. The Grell-Devenyi ensemble
195 cumulus scheme (Grell and Devenyi 2002) was used for D01 and D02. No cumulus
196 parameterization was used for D03. In addition, a 10-member ensemble forecast was
197 performed with the same physical parameterization schemes and domains as the control
198 simulation. The ensemble was generated by adding perturbations randomly sampled
199 from the default background error covariance of "cv3" in the WRF three-dimensional
200 variational data assimilation system (3DVar, Barker et al. 2004), similar to Meng and
201 Zhang (2007, 2008a, b, 2011). The domain-averaged standard deviations of perturbed
202 variables (0.56 m s^{-1} for u and v, 0.10 g kg^{-1} for q_v, 0.25 K for T, and 11 Pa for p')
203 were much smaller than the observational uncertainties.
204

205 *b. CI in the control simulation*

206 The control simulation successfully captured the initiation of the linear MCS and
207 the near-CI environment with acceptable timing and location errors. Following widely
208 used CI definitions based on radar observations (e.g., Kingsmill 1995; Weckwerth 2000;
209 Roberts and Rutledge 2003; Huang et al. 2017), in the current study, CI was defined
210 when radar echo first reached 35 dBZ, which then developed into a linear MCS. A weak
211 echo of 10 dBZ appeared at 2220 UTC 22 June (Fig. 7a) and reached 35 dBZ at 2240
212 UTC (Fig. 7b), which represented the initiation of convection. Newly initiated
213 convective cells merged together as they moved northeastward (Fig. 7c–e) and
214 gradually developed into a northwest–southeast-oriented convective line (Fig. 7f)
215 similar to the observations (Fig. 2e). In addition, the simulated sounding profile S2 (Fig.
216 8b, location denoted in Fig. 7f) at 0000 UTC 23 June located upstream of the linear
217 MCS closely resembled the Fuyang sounding (Fig. 5a). A prominent near-surface
218 temperature inversion and an elevated saturated layer (679–628 hPa) were revealed by
219 S2 in the simulation (Fig. 8b). The surface-based CAPE at S2 was 1538 J kg^{-1}, and
220 the inversion near the surface resulted in a surface-based CIN of 115 J kg^{-1}. Similar to
221 the Fuyang sounding, the elevated saturated layer greatly reduced the CIN of the parcel
222 lifted above the stable boundary layer (e.g., 12 J kg^{-1} at 850 hPa). The CI timing in the
223 control simulation was approximately 1 hour later than that in the observation, and the
224 CI location was approximately 100 km east of the observation. However, considering
225 the limitations of convection-permitting models in predicting the timing and location

of pristine elevated CIs shown by Stelten and Gallus (2017) and the similar convection morphology between simulation and observation during the CI, we believe that this simulation can reasonably be used to investigate CI mechanisms.

Similar to the observation, the simulated surface environment was unfavorable for surface-based CI. The simulated CI occurred within the weak uniform southerlies, and the surface temperature gradient was rather small before the CI (Fig. 9a, b). The magnitude of divergence on the bottom model level was less than 10^{-4} s^{-1}, which was much weaker than the convergence in a surface-based CI environment [e.g., 5×10^{-4} s^{-1} in Su and Zhai (2017)], indicating the absence of strong updrafts near the surface. Considering the weak near-surface lifting and the surface-based CIN of 50–100 J kg^{-1} that resulted from the temperature inversion near the surface, the convection could hardly originate from the surface. Due to the diurnal variation and the weakened temperature inversion, CIN reduced slightly at 2240 UTC 22 June (Fig. 9c, CI timing) but was still ~50 J kg^{-1}. Surface cold pools are often associated with surface-based convection initiation (Weckwerth and Parsons 2006), but in the present case, no strong cold pool was observed near the surface even 20 min after the CI (Fig. 9d). All the evidences suggested that the initiation in this case was elevated.

The simulated sounding at the CI location 20 minutes before the CI (S1 at 2220 UTC denoted in Fig. 7a) revealed a MAUL with a depth of 30 hPa (between 809 hPa and 778 hPa, ~2.0 km AGL) and a lapse rate of 6.4 K km^{-1} (Fig. 8a), which was greater than the moist adiabatic lapse rate. The vertical velocity averaged within the MAUL

247 over the red box denoted in Fig. 10a was 2.60 cm s^{-1}, which was broadly consistent
248 with the weak vertical motion of −3 to −10 μb s^{-1} at low levels observed in Trier et al.
249 (2017). In S1, the parcel lifted from the base of the MAUL (809 hPa) had a CAPE of
250 748 J kg^{-1} and an approximately negligible CIN (Fig. 8a). Based on parcel theory, this
251 indicates that weak and even imperceptible updrafts within the MAUL could overcome
252 the CIN and release the conditional instability. At the altitude of the MAUL (~2.0 km
253 AGL), there was a northwest–southeast-oriented nearly saturated (relative humidity
254 greater than 95%) band at 2200 UTC 22 June perpendicular to the strong low-level
255 southwesterly winds (Fig. 10a). This elevated nearly saturated band resulted in a narrow
256 area with negligible CIN (magnitude smaller than 0.5 J kg^{-1}, white contour) with a
257 length of ~150 km. The elevated nearly saturated band expanded at 2220 UTC, which
258 led to a wider area with negligible CIN (Fig. 10b). Several convective cells were
259 initiated in this area at 2240 UTC (Fig. 10c), and the associated nearly saturated band
260 gradually broke up due to the condensation from the convection (Fig. 10d).

261 Back trajectories of parcels released from the location of the first 10-dBZ echo at
262 2220 UTC at altitudes between 0.3 km and 2.3 km AGL were computed for 4 h using
263 the 5-min-resolution model output from the control simulation (Fig. 11). Trajectories
264 above ~1 km AGL were characterized as having sloping mesoscale ascent, whereas
265 there was no obvious lifting in near-surface trajectories, which reconfirmed that the
266 convection did not originate from the surface. Moreover, the horizontal distribution of
267 the trajectories revealed that the southwesterly winds were mainly above ~1 km AGL,

while the near-surface trajectories were more southerly, which was corroborated by the observation (Fig. 1b and Fig. 4a).

The difference between 1–2.3 km AGL and 0.3–1 km AGL trajectories (Fig. 11a) resulted in distinct evolutions of the diagnostic variables along the trajectories. CIN along the trajectories above 1 km AGL gradually decreased to negligible values as the CI was approached, while the CIN along near-surface trajectories only slightly decreased (Fig. 12a). For example, the CIN along the 1.7-km trajectory decreased from 30 J kg^{-1} to approximately 0 J kg^{-1} during the 4 h before CI, which suggested the formation of an elevated MAUL; however, the CIN along the 0.3-km AGL trajectory decreased only from 60 J kg^{-1} to 50 J kg^{-1} (Fig. 12a). The increase in relative humidity was broadly consistent with the decrease in CIN. During 2020–2220 UTC, the relative humidity along trajectories between 1.2–2.3 km AGL rapidly increased to near saturation (over 90%), while the near-surface relative humidity slightly increased but remained unsaturated (Fig. 12b). During the 4 hours prior to CI, CAPE along most trajectories slightly increased (Fig. 12c), indicating the relatively steady conditional instability before CI.

Notably, although the mesoscale vertical motion generally increased with height (Fig. 12d), the vertical velocity along trajectories did not vary monotonically with time as did other diagnostic variables. The vertical velocity varied between −2 and 10 cm s^{-1} without identifiable patterns, which indicated that the updraft underwent no regular change as initial convection was approached (before 2200 UTC). Without obvious

289 lifting mechanisms, CI seemed to be more dependent on the thermodynamic field that
290 was becoming increasingly conducive to CI. Given sufficient conditional instability, CI
291 could be largely dependent on the formation of the elevated MAUL.
292
293 *c. Formation mechanisms and characteristics of MAUL*
294 The formation of the elevated MAUL was further examined on a vertical cross
295 section taken along the low-level southwesterly winds perpendicular to the linear MCS
296 (cross-section path shown in Fig. 10b). The horizontal wind speed field along the cross
297 section featured a typical LLJ structure (Fig. 13a). There was cooling of ~ −0.6 K
298 between 2 and 3 km AGL, possibly related to the weak lifting (vertical velocity of ~5
299 cm s^{-1}) near the terminus of the LLJ. The cooling increased and extended both upward
300 and downward as the LLJ between 2–3 km AGL intensified (Fig. 13b). Moreover, the
301 high-moisture area signified by the surge of the equivalent potential temperature (θ_e)
302 near 2.0 km AGL was also gradually moving northeastward (Fig. 13c, d). The saturated[2]
303 layer located in the potential unstable environment (Fig. 13e, f) indicated the existence
304 of the elevated MAUL, especially when the initial convection was still absent (at 2100
305 UTC in Fig. 13e). This suggested that the elevated MAUL in the current case was an
306 important precondition for initial convection rather than simply the result of the
307 convection. Both the cooling and the moisture surge near the terminus of the LLJ

[2] Following the metrics in Bryan and Fritsch (2000), a grid point is considered saturated if the cloud water mixing ratio exceeds 0.01 g kg^{-1}.

contributed to the formation of MAUL, and convective cells were eventually generated in the elevated MAUL (Fig. 13b, d).

The contributions to the formation of the elevated MAUL from the budget of thermodynamic variables were quantitatively diagnosed by using equations of potential temperature and water vapor mixing ratio:

$$\frac{\partial \theta}{\partial t} = -\boldsymbol{V} \cdot \nabla_h \theta - w\frac{\partial \theta}{\partial z} + D_\theta \quad (1)$$

$$\frac{\partial q_v}{\partial t} = -\boldsymbol{V} \cdot \nabla_h q_v - w\frac{\partial q_v}{\partial z} + D_{q_v} \quad (2),$$

where D_θ and D_{q_v} are the diabatic forcing terms of potential temperature and water vapor mixing ratio. All terms in the equations were averaged horizontally over the domain indicated by the red box in Fig. 10a and vertically over model levels within the MAUL shown in Fig. 8a. Since the magnitude of the adiabatic term (sum of horizontal and vertical transport) was much larger than the diabatic term in both equations (Fig. 14), the thermodynamic process was nearly adiabatic in most of the time prior to CI (e.g., from 2120 to 2200 UTC). During the 1-h period before the first 10-dBZ echo appeared (2120–2220 UTC), there was a potential temperature decrease of 0.47 K (not shown), a water vapor increase of 0.47 g kg^{-1} (not shown) and a relative humidity increase from 92% to 97.5% (Fig. 14b). During 2120–2140 UTC, horizontal advection of potential temperature was the main contributor to the local cooling, while the vertical transport of potential temperature became stronger than the horizontal advection of potential temperature after 2140 UTC as the layer became saturated (Fig. 14a). In the local change of moisture (Fig. 14b), the horizontal advection of water vapor outweighed

329 the vertical transport most of the time (until 2200 UTC), during which the relative
330 humidity rapidly increased, which indicated that the local moisture accumulation was
331 mainly contributed by the horizontal moisture transport from upstream. This result was
332 somewhat different from cases in the U.S. Plains (Trier et al. 2014) where the vertical
333 moisture transport is typically more important in reducing negative buoyancy in the
334 near inflow to convection than the horizontal moisture transport. During the Meiyu
335 season in central eastern China from mid-June to mid-July, the southwesterly LLJ often
336 appears on the northwest edge of the subtropical high over the northwest Pacific Ocean
337 (Tao and Chen 1987), transporting rich moisture mainly horizontally from South China
338 Sea or East China Sea. It likely contains more moisture than the summertime LLJ air
339 in the U.S. plains originating in a hotter and drier region which makes the U.S. cases
340 require greater upward moisture transport to create a MAUL. To summarize, the
341 adiabatic cooling from the weak vertical ascent and the horizontal moisture transport
342 mainly contributed to the formation of the elevated saturated layer in the current case.
343 Near the CI location, the layer between 1–2 km AGL was potentially unstable
344 ($\partial\theta e/\partial z<0$, Fig. 13e, f). The weak ascent within the layer was likely to facilitate the
345 realization of the potential instability and eventually led to the formation of MAUL.
346 The layer-lifting process related to the release of potential instability was also
347 corroborated with the shallow stratiform clouds before CI observed in satellite images
348 (Fig. 3). Moreover, the moist static unstable environment near CI (Fig. 13e, f) suggested
349 that gravity waves or bores might not be lifting mechanisms.

Characteristics of the simulated MAUL in the weak-lifting environment of the present case were quite different from those in deep and intense updraft. Fig. 15a displays the horizontal distribution of the MAUL (a saturated[3] layer within which θ_e decreases with height). At 2200 UTC on 2 km AGL, the MAUL extended horizontally for approximately 200 km in length and 50 km in width, with the same northwest–southeast orientation as the convective line that developed downstream later. The horizontal width of 50 km was comparable to that of the MAUL examined near the gust front induced by a squall line (Bryan and Fritsch 2000). However, the vertical scale of the MAUL in this weak-lifting environment was quite different. Fig. 15b reveals the vertical thermodynamic conditions as the MAUL passed the grid point upstream of the CI location (the location of the grid point is denoted in Fig. 15a). The grid point was chosen upstream of the CI location to avoid the influence of strong updrafts associated with deep convection. The vertical distribution of $\frac{\partial \theta_e}{\partial z}$ reconfirmed the existence of the potential unstable layer above 1 km AGL and the MAUL located between 2 and 3 km AGL. The MAUL depth of 1 km was much shallower than the MAUL depth in a strong-lifting environment, which is generally ~3 km (Bryan and Fritsch 2000). Moreover, the lapse rate of temperature within the MAUL was −4 to −6 K km^{-1} (not shown) and was weaker than the lapse rate of −5 to −8 K km^{-1} near the gust front (Bryan and Fritsch 2000). With regard to the temporal scale, the MAUL persisted for nearly 80 min from

[3] Following the metrics in Bryan and Fritsch (2000), a grid point is considered saturated if the cloud water mixing ratio exceeds 0.01 g kg^{-1}.

2150 to 2310 UTC on an individual grid (Fig. 15b), which was longer than the duration of 30–45 min in a strong-lifting environment (Bryan and Fritsch 2000). In the early stage of the MAUL, there was weak vertical ascent (0–5 cm s^{-1}) within the MAUL, which might lead to the lifting of the saturated layer during 2220–2230 UTC. Subsequently, the vertical ascent became weaker and, as a result, the MAUL began to weaken with a smaller magnitude of the lapse rate of θ_e and eventually collapsed at 2310 UTC.

It is interesting that the MAUL could be sustained even without strong mesoscale ascent, which has been considered an essential factor in the maintenance of MAULs. Two factors were favorable for sustaining the MAUL in the present case. One is the sufficient horizontal moisture transport associated with the LLJ. The other is the small depth of the MAUL; a MAUL can be sustained only when the environmental mesoscale ascent generates instability faster than it can be removed by convective overturning as a result of buoyancy-driven velocity (Bryan and Fritsch 2000). Deeper MAULs, which induce a stronger buoyancy-driven vertical velocity, require stronger environmental vertical ascents to keep the MAULs from being destroyed (Barnes 2008). This behavior suggests that when the MAUL depth is shallow, weak vertical ascent will be sufficient to balance the buoyancy-driven vertical velocity and sustain the MAUL.

d. CI predictability

To understand the predictability of the elevated CI in the weak-lifting environment,

390 the variability of CI timing and location in a 10-member ensemble forecast was
391 examined. Similar to the CI definition mentioned in section 4b, for each ensemble
392 member the CI timing for the target MCS was defined as the time when the radar echo
393 first reached 35 dBZ, which then developed into a contiguous or quasi-contiguous band
394 of over 40-dBZ reflectivity with a northwest–southeast orientation and a length of at
395 least 50 km before 0130 UTC 23 June in the area of interest (the area of Fig. 16). The
396 CI was reproduced in eight out of ten ensemble members (members 01, 02, 04, 06, 07,
397 08, 09 and 10), which indicated the high predictability (80%) of CI in this case (Fig.
398 16). There was considerable variability in the timing and location of CI members.
399 Including the control simulation, the CI timing ranged from 1930 UTC (member 10) to
400 2300 UTC (member 01), with a median of CI timing at 2220 UTC, and the CI location
401 uncertainty was generally within ~100 km.

402 Whether having an elevated MAUL or not was the major difference between CI
403 and non-CI members. At 20 min before CI timing, all CI members exhibited an elevated
404 MAUL at 2 km AGL (Fig. 17a, b, d, and f–j). The MAULs in CI members generally
405 had a depth of 1 km, similar to the control simulation, and persisted for 40–120 min on
406 individual grids (not shown). These shallow but long-lasting MAULs in CI members
407 were vastly important since CI could possibly occur at any location within the MAUL
408 during its lifetime. In contrast, all of the non-CI ensemble members failed to produce
409 MAULs (Fig. 17c and e). This finding supported the possibility that CI could be mainly
410 determined by the existence of a MAUL. Strong fine-scale dynamic lifting may not be

411 necessary in this elevated CI event. A comparison between typical CI members
412 (members 02 and 08) with similar CI timing and non-CI members (member 03 and 05)
413 (Fig. 18) showed that no obvious difference of vertical velocity in the general weak-
414 lifting environment over the exit region of LLJ (approximately 1–3 km AGL, 50–170
415 km in SW-NE distance) could be identified to distinguish CI members from non-CI
416 members.
417
418 **5. Summary**
419 This study investigated an elevated CI event in central eastern China in the early
420 morning on 23 June 2016. The CI occurred near the terminus of an LLJ in a weak-
421 lifting environment far from a surface front. This elevated CI resulted in a linear MCS
422 that gradually developed into a surface-based MCS and spawned an intensive supercell
423 in the afternoon, which produced a severe EF4 tornado that killed 98 people.
424 Both observations and simulations suggested that this CI event was elevated and
425 that the MAUL greatly facilitated CI by providing approximately negligible CIN.
426 Surface observations and the sounding environment showed that there was no obvious
427 surface boundary near CI locations and that the near-surface CIN was larger than that
428 at ~2 km above the ground due to the near-surface temperature inversion at night and
429 an elevated nearly saturated layer (MAUL). Back-trajectory analysis based on
430 numerical simulation demonstrated the sloping ascent path before the onset of CI and
431 reconfirmed that the convective updraft did not originate from the surface and the

existence of weak vertical ascent before the elevated CI. Along the parcel trajectories at low levels, CIN gradually decreased to negligible values and relative humidity increased nearly to saturation, which led to the formation of the elevated MAUL. However, the vertical velocity did not increase monotonically with time as CI was approached; rather, it was quite weak (lower than 12 cm s^{-1}) and oscillated without an identifiable pattern. This condition suggested that the CI was more likely determined by the formation of the elevated MAUL than by the evolution of vertical velocity.

The formation mechanisms and characteristics of the MAUL in this case were investigated using numerical simulations. The elevated saturation was promoted by moisture surge and cooling near the LLJ terminus. Specifically, the increase in moisture was mainly contributed by horizontal moisture transport associated with the LLJ, while the cooling was mainly from adiabatic cooling associated with weak vertical motion rather than horizontal transport of potential temperature. Compared with MAULs in strong-lifting environments, the simulated MAUL in this weak-lifting environment had a shallower depth of 1 km, a much weaker vertical ascent of 0–5 cm s^{-1}, a weaker lapse rate of temperature of −4 to −6 K km^{-1}, and a longer duration of 80 min. The shallow depth of the MAUL and the sufficient horizontal moisture transport were substantial factors in sustaining the MAUL in the weak-lifting environment.

The predictability of this elevated CI in the weak-lifting environment was investigated using a 10-member ensemble forecast with an ensemble spread much smaller than the observational error. The probability of CI was approximately 80%. The

453 elevated MAUL, which was generally long lasting, was possibly a decisive condition
454 for the CI in this event.
455
456 **Acknowledgements**
457 This work was sponsored by the National Natural Science Foundation of China (Grants
458 41425018 and 41875051) and the Ministry of Science and Technology of China (Grant
459 2013CB430104).
460
461 **References**
462 Barker, D. M., W. Huang, Y-R. Guo, A. J. Bourgeois, and Q. N. Xiao, 2004: A three-
463 dimensional variational data assimilation system for MM5: Implementation and
464 initial results. *Mon. Wea. Rev.*, **132**, 897–914.
465 Barnes, G. M., 2008: Atypical thermodynamic profiles in hurricanes. *Mon. Wea. Rev.*,
466 **136**, 631–643, doi:10.1175/2007MWR2033.1.
467 Bentley, M. L., and T. L. Mote, 1998: A climatology of derecho-producing mesoscale
468 convective systems in the central and eastern United States, 1986–95. Part I:
469 Temporal and spatial distribution. *Bull. Amer. Meteor. Soc.*, **79**, 2527–2540,
470 doi:10.1175/1520-0477(1998)079,2527:ACODPM.2.0.CO;2.
471 Bryan, G. H., 2005: Spurious convective organization in simulated squall lines owing
472 to moist absolutely unstable layers. *Mon. Wea. Rev.*, **133**, 1978–1997,
473 doi:10.1175/MWR2952.1.

474 Bryan, G. H., and J. M. Fritsch, 2000: Moist absolute instability: The sixth static
475 stability state. *Bull. Amer. Meteor. Soc.*, **81**, 1207–1230, doi:10.1175/1520-
476 0477(2000)081,1287: MAITSS.2.3.CO;2.
477 Carbone, R. E., J. D. Tuttle, D. A. Ahijevych, and S. B. Trier, 2002: Inferences of
478 predictability associated with warm season precipitation episodes. *J. Atmos. Sci.*,
479 **59**, 2033–2056, doi:10.1175/1520-0469(2002)059,2033:IOPAWW.2.0.CO;2.
480 Chen, H., R. Yu, J. Li, W. Yuan, and T. Zhou, 2010: Why nocturnal long-duration
481 rainfall presents an eastward-delayed diurnal phase of rainfall down the Yangtze
482 River Valley. *J. Climate*, **23**, 905–917, doi:10.1175/2009JCLI3187.1
483 Colman, B. R., 1990: Thunderstorms above frontal surfaces in environments without
484 positive CAPE. Part I: A climatology. *Mon. Wea. Rev.*, **118**, 1103–1121,
485 doi:10.1175/ 1520-0493(1990)118,1103:TAFSIE.2.0.CO;2.
486 Corfidi, S. F., S. J. Corfidi, and D. M. Schultz, 2008: Elevated convection and
487 castellanus: Ambiguities, significance, and questions. *Wea. Forecasting*, **23**, 1280–
488 1330, doi:10.1175/ 2008WAF2222118.1.
489 Davis, C. A., K. W. Manning, R. E. Carbone, S. B. Trier, and J. D. Tuttle, 2003:
490 Coherence of warm-season continental rainfall in numerical weather prediction
491 models. *Mon. Wea. Rev.*, **131**, 2667-2679.
492 Degelia, S.K., X. Wang, D.J. Stensrud, and A. Johnson, 2018: Understanding the impact
493 of radar and in situ observations on the prediction of a nocturnal convection
494 initiation event on 25 June 2013 using an ensemble-based multiscale data

assimilation system. *Mon. Wea. Rev.*, **146**, 1837–1859, https://doi.org/10.1175/MWR-D-17-0128.1

Du, Y., Q. Zhang, Y. Chen, Y. Zhao, and X. Wang, 2014: Numerical Simulations of Spatial Distributions and Diurnal Variations of Low-Level Jets in China during Early Summer. J. Climate, 27, 5747–5767, https://doi.org/10.1175/JCLI-D-13-00571.1

Gebauer, J.G., A. Shapiro, E. Fedorovich, and P. Klein, 2018: Convection Initiation Caused by Heterogeneous Low-Level Jets over the Great Plains. *Mon. Wea. Rev.*, **146**, 2615–2637, https://doi.org/10.1175/MWR-D-18-0002.1

Geerts, B., and Coauthors, 2017: The 2015 Plains Elevated Convection At Night field project. *Bull. Amer. Meteor. Soc.*, **98**, 767–786, doi:10.1175/BAMS-D-15-00257.1.

Grell, G. A., and D. Devenyi, 2002: A generalized approach to parameterizing convection combining ensemble and data assimilation techniques. *Geophys. Res. Lett.*, **29**(14), doi: 10.1029/2002GL015311.

He, Z., Q. Zhang, L. Bai, and Z. Meng, 2017: Characteristics of mesoscale convective systems in central East China and their reliance on atmospheric circulation patterns, *Int. J. Climatol*, **37(7)**, 3276–3290.

Hong, S.-Y., and J.-O. J. Lim, 2006: The WRF single-moment 6-class microphysics scheme (WSM6). *J. Korean Meteor. Soc.*, **42**, 129–151.

Hong, S.-Y., Y. Noh, and J. Dudhia, 2006: A new vertical diffusion package with an explicit treatment of entrainment processes. *Mon. Wea. Rev.*, **134**, 2318–

2341, https://doi.org/10.1175/MWR3199.1.

Huang, Y., Z. Meng, J. Li, W. Li, L. Bai, M. Zhang, and X. Wang, 2017: Distribution and variability of satellite-derived signals of isolated convection initiation events over central eastern China. *Journal of Geophysical Research: Atmospheres*, **122**:21, 11,357-11,373.

Kingsmill, D. E. (1995). Convection initiation associated with a sea-breeze front, a gust front, and their collision. Monthly Weather Review, **123**, 2913–2933.

Kis, A. K., and J. M. Straka, 2010: Nocturnal tornado climatology. *Wea. Forecasting*, **25**, 545–561, https://doi.org/10.1175/2009WAF2222294.1.

Koch, S.E. and C. O'Handley, 1997: Operational Forecasting and Detection of Mesoscale Gravity Waves. *Wea. Forecasting*, **12**, 253–281, https://doi.org/10.1175/1520-0434(1997)012<0253:OFADOM>2.0.CO;2

Maddox, R. A., 1980: Mesoscale convective complexes. *Bull. Amer. Meteor. Soc.*, **61**, 1374–1387, doi:10.1175/ 1520-0477(1980)061,1374:MCC.2.0.CO;2.

Marsham, J. H., S. B. Trier, T. M. Weckwerth and J. W. Wilson, 2011: Observations of elevated convection initiation leading to a surface-based squall-line during 13 June IHOP_2002, *Mon. Wea. Rev.*, **139**, 247 -271.

Meng, Z., and F. Zhang, 2007: Tests of an ensemble Kalman filter for mesoscale and regional-scale data assimilation. Part II: Imperfect model experiments. *Mon. Wea. Rev.*, **135**, 1403–1423, doi: https://doi.org/10.1

Meng, Z., and F. Zhang, 2008a: Test of an ensemble Kalman filter for mesoscale and

regional-scale data assimilation. Part III: Comparison with 3DVar for a real-data case study. *Mon. Wea. Rev.*, **136**, 522–540, doi: https://doi.org/10.1175/2007MWR2106.1.

Meng, Z., and F. Zhang, 2008b: Test of an ensemble Kalman filter for mesoscale and regional-scale data assimilation. Part IV: Comparison with 3DVar in a month-long experiment. *Mon. Wea. Rev.*, **136**, 3671–3682, doi: https://doi.org/10.1175/2008MWR2270.1.

Meng, Z., and F. Zhang, 2011: Limited-area ensemble-based data assimilation. *Mon. Wea. Rev.*, **139**, 2025–2045, doi: https://doi.org/10.1175/2011MWR3418.1

Meng, Z., L. Bai, M. Zhang, Z. Wu, Z. Li, M. Pu, Y. Zheng, X. Wang, D. Yao, M. Xue, K. Zhao, Z. Li, S. Peng, and L. Li, 2018: The deadliest tornado (EF4) in the past 40 years in China. *Wea. Forecasting*, **33**, 693–713, https://doi.org/10.1175/WAF-D-17-0085.1

Meng, Z., D. Yan, and Y. Zhang, 2013: General features of squall lines in East China. *Mon. Wea. Rev.*, **141**, 1629–1647.

Mlawer, E. J., S. J. Taubman, P. D. Brown, M. J. Iacono, and S. A. Clough, 1997: Radiative transfer for inhomogeneous atmospheres: RRTM, a validated correlated-k model for the longwave. *Journal of Geophysical Research: Atmospheres*, **102** (D14), 16 663–16 682.

Parker, M. D., 2008: Response of simulated squall lines to low-level cooling. *J. Atmos. Sci.*, **65**, 1323–1341, doi:10.1175/2007JAS1507.1.

Reif, D. W., and H. B. Bluestein, 2017: A 20-year climatology of nocturnal convection initiation over the central and southern Great Plains during the warm season. *Mon. Wea. Rev.*, **145**, 1615–1639, doi:10.1175/MWR-D-16-0340.1.

Roberts, R. D., and S. Rutledge, 2003: Nowcasting storm initiation and growth using GOES-8 and WSR-88D data, *Wea. Forecasting*, **18**, 562–584, doi:10.1175/1520-0434(2003)018,0562: NSIAGU.2.0.CO;2.

Shapiro, A., E. Fedorovich, and J.G. Gebauer, 2018: Mesoscale Ascent in Nocturnal Low-Level Jets. *J. Atmos. Sci.*, **75**, 1403–1427, https://doi.org/10.1175/JAS-D-17-0279.1

Skamarock, W., and Coauthors, 2008: A description of the Advanced Research WRF Version 3, NCAR technical note, Mesoscale and Microscale Meteorology Division. National Center for Atmospheric Research, Boulder, Colorado, USA.

Stelten, S. and W.A. Gallus, 2017: Pristine nocturnal convective initiation: A climatology and preliminary examination of predictability. *Wea. Forecasting*, **32**, 1613–1635, https://doi.org/10.1175/WAF-D-16-0222.1

Su, T. and G. Zhai, 2017: The Role of Convectively Generated Gravity Waves on Convective Initiation: A Case Study. *Mon. Wea. Rev.*, **145**, 335–359, https://doi.org/10.1175/MWR-D-16-0196.1

Tao S Y, Chen L X. 1987. A review of recent research on the East Asian summer monsoon in China[M]//Chang C P, Krishnamurti T N. Monsoon Meteorology. London: Oxford University Press, 60-92.

579 Trier, S.B., C.A. Davis, D.A. Ahijevych, and K.W. Manning, 2014: Use of the Parcel
580 Buoyancy Minimum (Bmin) to Diagnose Simulated Thermodynamic
581 Destabilization. Part II: Composite Analysis of Mature MCS Environments. *Mon.*
582 *Wea. Rev.*, **142**, 967–990, https://doi.org/10.1175/MWR-D-13-00273.1
583 Trier, S. B., C. A. Davis, D. A. Ahijevych, M. L. Weisman, and G.
584 H. Bryan, 2006: Mechanisms supporting long-lived episodes of propagating
585 nocturnal convection within a 7-day WRF Model simulation. *J. Atmos.*
586 *Sci.*, **63**, 2437–2461, doi: https://doi.org/10.1175/JAS2768.1.
587 Trier, S.B., J.W. Wilson, D.A. Ahijevych, and R.A. Sobash, 2017: Mesoscale vertical
588 motions near nocturnal convection initiation in PECAN. *Mon. Wea. Rev.*, **145**,
589 2919–2941, https://doi.org/10.1175/MWR-D-17-0005.1
590 Wallace, J. M., 1975: Diurnal variations in precipitation and thunderstorm frequency
591 over the conterminous United States. *Mon. Wea. Rev.*, **103**, 406–419,
592 doi:10.1175/1520-0493(1975)103,0406: DVIPAT.2.0.CO;2.
593 Weckwerth, T. M. (2000). The effect of small‐scale moisture variability on
594 thunderstorm initiation. Monthly Weather Review, **128**, 4017–4030.
595 Weckwerth, T.M. and D.B. Parsons, 2006: A review of convection initiation and
596 motivation for IHOP_2002. *Mon. Wea. Rev.*, **134**, 5–22,
597 https://doi.org/10.1175/MWR3067.1
598 Weckwerth, T. M., and Coauthors, 2004: An overview of the International H2O Project
599 (IHOP_2002) and some preliminary highlights. *Bull. Amer. Meteor. Soc.*, **85**, 253–

277, doi:10.1175/BAMS-85-2-253.

Wilson, J. W., and R. D. Roberts, 2006: Summary of convective storm initiation and evolution during IHOP: Observational and modeling perspective. *Mon. Wea. Rev.*, **134**, 23–47, doi:10.1175/ MWR3069.1.

Wilson, J.W., S.B. Trier, D.W. Reif, R.D. Roberts, and T.M. Weckwerth, 2018: Nocturnal Elevated Convection Initiation of the PECAN 4 July Hailstorm. *Mon. Wea. Rev.*, **146**, 243–262, https://doi.org/10.1175/MWR-D-17-0176.1

Whiteman, C.D., X. Bian, and S. Zhong, 1997: Low-Level Jet Climatology from Enhanced Rawinsonde Observations at a Site in the Southern Great Plains. J. Appl. Meteor., 36, 1363–1376, https://doi.org/10.1175/1520-0450(1997)036<1363:LLJCFE>2.0.CO;2

Yu, R., T. Zhou, A. Xiong, Y. Zhu, and J. Li, 2007: Diurnal variations of summer precipitation over contiguous China, *Geophys. Res. Lett.*, **34**, L01704, doi:10.1029/2006GL028129.

Zheng, L.-L., J.-H. Sun, X.-L. Zhang, and C.-H. Liu, 2013: Organizational modes of mesoscale convective systems over central east China. *Wea. Forecasting*, **28**, 1081–1098, doi:10.1175/WAF-D-12-00088.1.

Zhu, X., and J. Zhu, 2004: New generation weather radar network in China (in Chinese with English abstract). *Mater. Sci. Technol.*, **32**, 255–258.

Figure captions

Fig.1 (a) Mosaics of composite radar reflectivity (dBZ) at 0000 UTC 23 June in central eastern China; the location of the Fuyang radar is marked with a blue cross; the target MCS and the provinces discussed in the text are shown on the map; the distance length scale is given at the bottom left. (b) Synoptic environment reflected by ECMWF HRES analysis at 0000 UTC 23 June including 500-hPa geopotential height (contoured in blue every 40 gpm) and 850-hPa horizontal wind speed (shaded), 850-hPa wind vector (barb=5 m s^{-1}, half barb=2.5 m s^{-1}), locations of the surface front and surface high and low pressure (denoted by the front symbols "H" and "L"); the red line indicates the location of the linear convective system at 0000 UTC 23 June.

Fig.2 Composite radar reflectivity (shaded in dBZ) of the Fuyang radar at (a) 2131 UTC, (b) 2228 UTC, (c) 2257 UTC, and (d) 2354 UTC 22 June and (e) 0051 UTC and (f) 0148 UTC 23 June. The location of the Fuyang radiosonde is given in (d). Initial convective cells discussed in the text are circled in red in (a). Anhui and Jiangsu provinces (discussed in the text) are marked in (a) and (f). The time of local sunrise was 2109 UTC (0509 LST).

Fig.3 Composite true-color images from Himawari-8 at (a) 2100 UTC, (b) 2110 UTC, (c) 2120 UTC and (d) 2130 UTC 22 June. The linear-organized cumulus cloud cells are circled in red in (c) and (d).

Fig.4 Surface pressure (contoured in blue every 0.5 hPa), surface wind vector (barb=2 m s^{-1}, half barb=1 m s^{-1}), surface temperature (text in red) and surface dewpoint temperature (text in blue) at (a) 2050 UTC, (b) 2110 UTC, (c) 2130 UTC, and (d) 2150 UTC 22 June. The shading denotes the composite reflectivity from the Fuyang radar (dBZ). Time series of surface pressure at station I2570 (green) and I2571 (purple) with locations given in (c) are shown in (e) with CI timing marked on the lower time axis. The pressure trace of a gravity wave from Koch and O'Handley (1997) adapted from their Fig. 18e is also shown in (e) in red with corresponding time (UTC) shown on the upper time axis for reference.

Fig. 5 Skew T–log p (a) and hodograph (b) diagrams of the Fuyang radiosonde (the red cross in Fig. 2d) at 0000 UTC 23 June 2016. (a) The ambient temperature and dewpoint are represented by the solid black and blue lines, respectively; parcels that ascend undiluted from the surface and 850 hPa are shown by the solid and dashed red lines, respectively; the wind profile is shown on the right side (barb=4 m s^{-1}, half barb=2 m s^{-1}, flag=20 m s^{-1}). (b) The velocities at certain pressure levels (hPa) are marked in red circles in the hodograph. CAPE, CIN and LFC of parcels lifted from different levels are given on the left in (a).

Fig.6 Terrain height (shaded; unit: m) and domains used for the control simulation as

well as ensemble forecasts.

Fig.7 Model-derived composite radar reflectivity (shaded in dBZ) in domain 3 (horizontal resolution of 3 km) of the control simulation at (a) 222 0 UTC, (b) 2240 UTC, (c) 2300 UTC, (d) 2320 UTC, and (e) 2340 UTC 22 June and (f) 0000 UTC 23 June. The simulated results hereafter are all from domain 3 (horizontal resolution of 3 km). The weak echo discussed in the text is circled in red in (a). Black crosses in (a) and (f) indicate locations of sounding profiles analyzed in Fig. 8. The area of radar observation in Fig. 2a is given as the gray box in (a).

Fig. 8 Skew T–log p diagrams of sounding derived from the control simulation at (a) 2220 UTC 22 June at S1 (black cross in Fig. 7a) and (b) 0000 UTC 23 June at S2 (black cross in Fig.7f). The ambient temperature and dewpoint are represented by the solid black and blue lines, respectively. In (a) S1, parcels that ascend undiluted from the surface and the base of MAUL are shown by the solid and dashed red lines, respectively; In (b) S2, parcels that ascend undiluted from the surface and 850 hPa are shown by the solid and dashed red lines, respectively. The wind profile is shown on the right side (barb=4 m s^{-1}, half barb=2 m s^{-1}, flag=20 m s^{-1}). CAPE, CIN and LFC of parcels lifted from different levels are given on the left.

Fig.9 Divergence (shaded every 10^{-5} s^{-1}; blue for convergence and red for divergence), CIN (contoured in dashed blue every 50 J kg^{-1}) and horizontal wind vector (barb=5 m s^{-1}, half barb=2.5 m s^{-1}) at the bottom model level, surface temperature (contoured in solid black every 1°C) and 35-dBZ contour of composite radar reflectivity (solid red) in the control simulation at (a) 2200 UTC, (b) 2220 UTC, (c) 2240 UTC and (d) 2300 UTC 22 June. The first convective cell reaching 35 dBZ is denoted in (c) as CI. The location of S1 given in (b) is the same as in Fig. 7a.

Fig.10 Relative humidity (shaded every 5%), 0.5 J kg^{-1} CIN (contoured in white), horizontal wind vector (barb=5 m s^{-1}, half barb=2.5 m s^{-1}) and potential temperature (contoured in dash black every 0.5 K) at 2.0 km AGL and the 35-dBZ contour (solid red) of composite radar reflectivity (solid red) in the control simulation at (a) 2200 UTC, (b) 2220 UTC, (c) 2240 UTC and (d) 2300 UTC 22 June. The location of S1 is the same as in Fig. 7a, and the cross section in Fig. 11a and Fig. 13 is given in (b). The red box denotes the area used for diagnosing the area-averaged transport of water vapor mixing ratio and potential temperature in Fig. 14.

Fig.11 (a) Vertical distributions of 4-h back trajectories of parcels released from the 10-dBZ radar echo at 2220 UTC with different heights (0.3–2.3 km AGL; colors correspond to different heights as shown in the top-right box) along the plane of the cross section in Fig. 10b; also shown are potential instability ($\partial\theta_e/\partial z$, shaded every 2 K km^{-1}), model-derived composite radar reflectivity (contoured in green at 5-dBZ intervals) and horizontal wind speed along the plane of the cross section (contoured in

solid black every 1 m s^{-1}) at 2220 UTC 22 June. (b) Horizontal distributions of the same parcel trajectories as in (a); also shown are relative humidity (shaded at 5% intervals), model-derived composite radar reflectivity (contoured in red at 5-dBZ intervals) and potential temperature (contoured in black dashes every 0.5 K) at 2.0 km AGL at 2220 UTC 22 June.

Fig.12 (a) CIN (J kg^{-1}), (b) relative humidity (%), (c) CAPE (J kg^{-1}) and (d) vertical velocity (cm s^{-1}) along the color-coded trajectories plotted in Fig. 11a. The black dashed line indicates the time (2200 UTC 22 June) when the first 5-dBZ echo appeared.

Fig.13 Vertical cross sections along the SW–NE transect in Fig. 10b of temperature perturbation (shaded at 0.2-K intervals), model-derived radar reflectivity (contoured in green at 5-dBZ intervals), horizontal wind speed along the plane of the cross section (contoured in solid black every 1 m s^{-1}) and circulation vectors in the plane of the cross section at (a) 2100 UTC and (b) 2220 UTC 22 June; the reference state used to compute the temperature perturbation has the same lapse rate (0.0065 K m^{-1} below 11 km) as the U.S. Standard Atmosphere and a sea-level temperature of 301 K from this current case. The second row shows the relative humidity (shaded at 5% intervals), model-derived radar reflectivity (contoured in green at 5-dBZ intervals), equivalent potential temperature (contoured in red every 2 K) and circulation vectors in the plane of the cross section at (c) 2100 UTC and (d) 2220 UTC 22 June. The third row shows the potential instability ($\partial\theta_e/\partial z$, shaded every 2 K km^{-1}), model-derived radar reflectivity (contoured in green at 5-dBZ intervals), cloud water mixing ratio (0.01 g kg^{-1} contour in solid brown), horizontal wind speed along the plane of the cross section (contoured in solid black every 1 m s^{-1}) and circulation vectors in the plane of the cross section at (e) 2100 UTC and (f) 2220 UTC 22 June. The reference vector is given at the bottom right and denotes a horizontal velocity of 10 m s^{-1} and a vertical velocity of 10 cm s^{-1}. The jet axes of the LLJ mentioned in the text are qualitatively denoted by the bold black dashed lines in (a) and (b).

Fig. 14 (a) Evolution of the area-averaged horizontal advection ($-\boldsymbol{V}\cdot\nabla_h\theta$, solid blue), vertical transport ($-w\frac{\partial\theta}{\partial z}$, solid red), diabatic term (D_θ, solid orange) and adiabatic term ($-\boldsymbol{V}\cdot\nabla_h\theta - w\frac{\partial\theta}{\partial z}$, solid black) of potential temperature within the subsequent MAUL (unit: 10^{-5} K s^{-1}) on 22 June. (b) is similar to (a) except for the water vapor mixing ratio (unit: 10^{-4} g kg^{-1} s^{-1}). The evolution of the area-averaged relative humidity within the subsequent MAUL is also plotted as the dashed green line in (b). The area used for averaging is denoted as the red box in Fig. 10a.

Fig.15 Temporal and spatial scale of the simulated MAUL. (a) Potential instability ($\partial\theta_e/\partial z$, shaded every 2 K km^{-1}), cloud water mixing ratio (0.01 g kg^{-1} contour in solid brown) and horizontal wind vector (barb=5 m s^{-1}, half barb=2.5 m s^{-1}) at 2 km

AGL at 2200 UTC 22 June. The CI location (first 35-dBZ echo at 2240 UTC 22 June) is denoted by the green cross. (b) Time series of vertical conditions at the grid point denoted by the brown cross in (a), potential instability ($\partial\theta_e/\partial z$, shaded every 2 K km^{-1}), cloud water mixing ratio (0.01 g kg^{-1} contour in solid brown) and 20-min-averaged vertical velocity (contoured in solid black for positive and negative in black dashes every 0.05 m s^{-1}). The CI timing (2240 UTC 22 June) is marked in black dashes in (b).

Fig.16 Model-derived (d03) composite radar reflectivity (shaded in dBZ) of the 10 ensemble members (a)–(j). CI members (red label) are plotted at respective CI timing, and non-CI members (blue label) are plotted at 2220 UTC 22 June for comparison.

Fig. 17 Distribution of elevated saturated area 20 min before CI including relative humidity (shaded every 5%), horizontal wind vector (barb=5 m s^{-1}, half barb=2.5 m s^{-1}), potential instability ($\partial\theta e/\partial z$, contoured in solid black every 2 K km^{-1}) and cloud water mixing ratio (solid white, contours of 0.01 g kg^{-1}) at 2.0 km AGL in 10 ensemble members (a)–(j). The solid black lines in (b), (c), (e) and (h) indicate the SW–NE path of the cross section in Fig. 18. The CI locations shown in Fig. 16 are marked as red crosses.

Fig. 18 Vertical cross sections along the SW–NE transect of typical CI and non-CI members in Fig. 17b, c, e and h, including relative humidity (shaded every 5%), horizontal wind speed along the plane of the cross section (contoured in solid black every 2 m s^{-1}), and 20-min-averaged vertical velocity (contoured in blue with positive (> 2 cm s^{-1}) in solid lines and negative (< -2 cm s^{-1}) in dashes every 4 cm s^{-1}) in (a) member 02 at 2210 UTC 22 June, (b) member 03 at 2200 UTC 22 June, (c) member 08 at 2200 UTC 22 June and (d) member 05 at 2200 UTC 22 June.

Figures

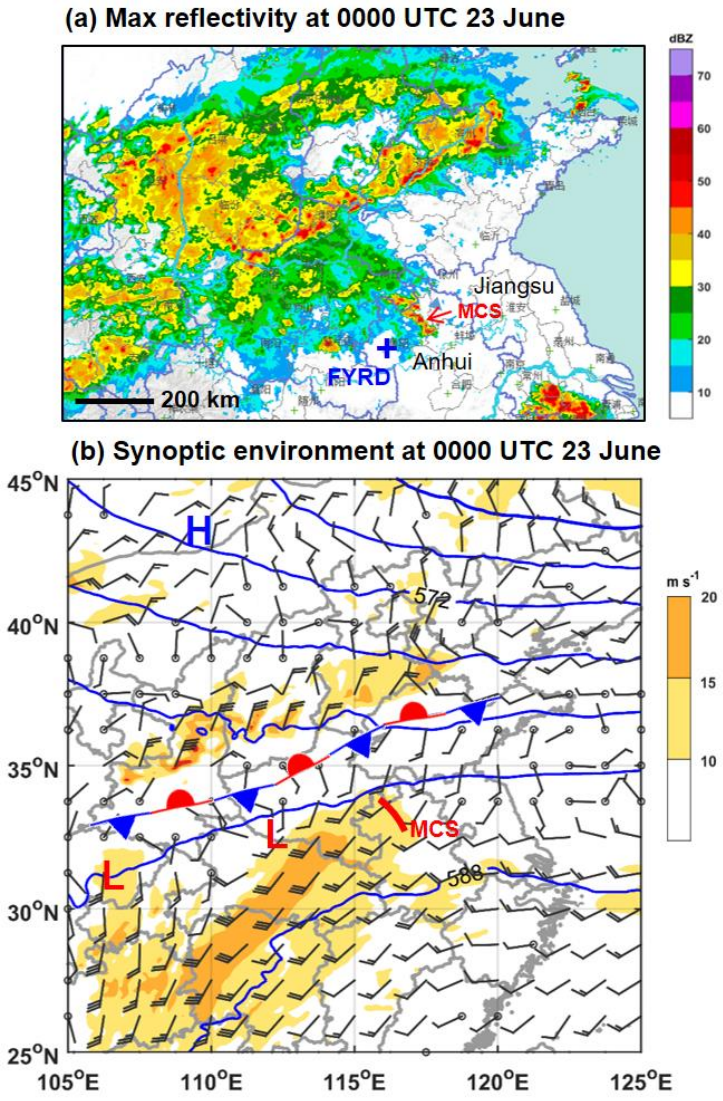

Fig.1 (a) Mosaics of composite radar reflectivity (dBZ) at 0000 UTC 23 June in central eastern China; the location of the Fuyang radar is marked with a blue cross; the target MCS and the provinces discussed in the text are shown on the map; the distance length scale is given at the bottom left. (b) Synoptic environment reflected by ECMWF HRES analysis at 0000 UTC 23 June including 500-hPa geopotential height (contoured in blue every 40 gpm) and 850-hPa horizontal wind speed (shaded), 850-hPa wind vector (barb=5 m s^{-1}, half barb=2.5 m s^{-1}), locations of the surface front and surface high and low pressure (denoted by the front symbols "H" and "L"); the red line indicates the location of the linear convective system at 0000 UTC 23 June.

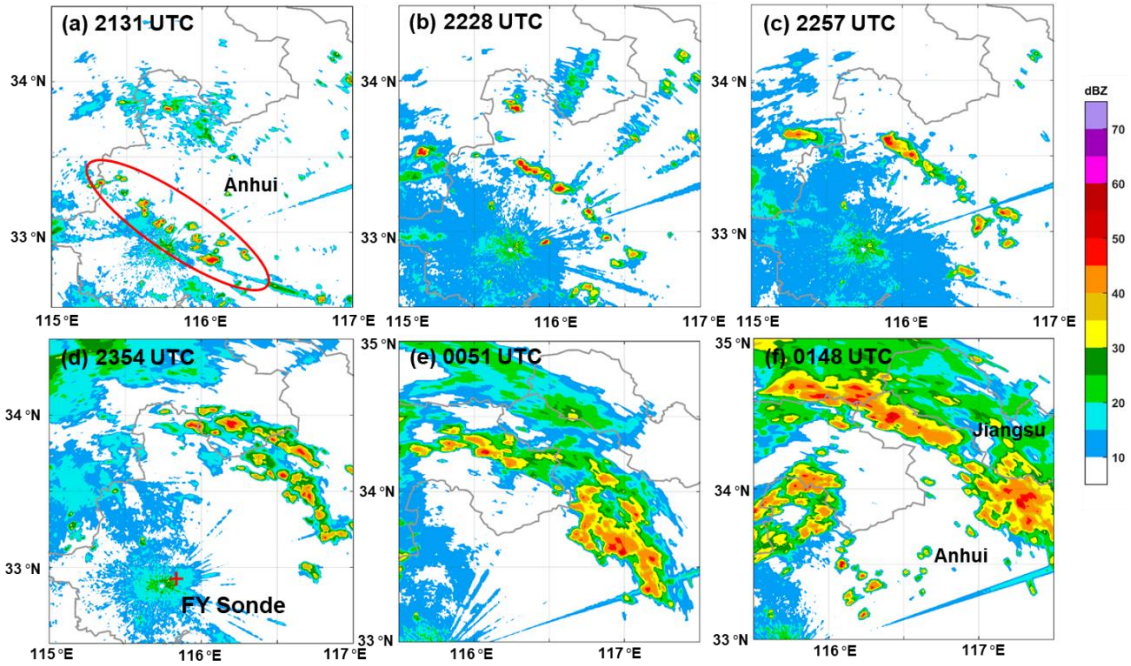

Fig.2 Composite reflectivity (shaded in dBZ) of the Fuyang radar at (a) 2131 UTC, (b) 2228 UTC, (c) 2257 UTC, and (d) 2354 UTC 22 June and (e) 0051 UTC and (f) 0148 UTC 23 June. The location of the Fuyang radiosonde is given in (d). Initial convective cells discussed in the text are circled in red in (a). Anhui and Jiangsu provinces (discussed in the text) are marked in (a) and (f). The time of local sunrise was 2109 UTC (0509 LST).

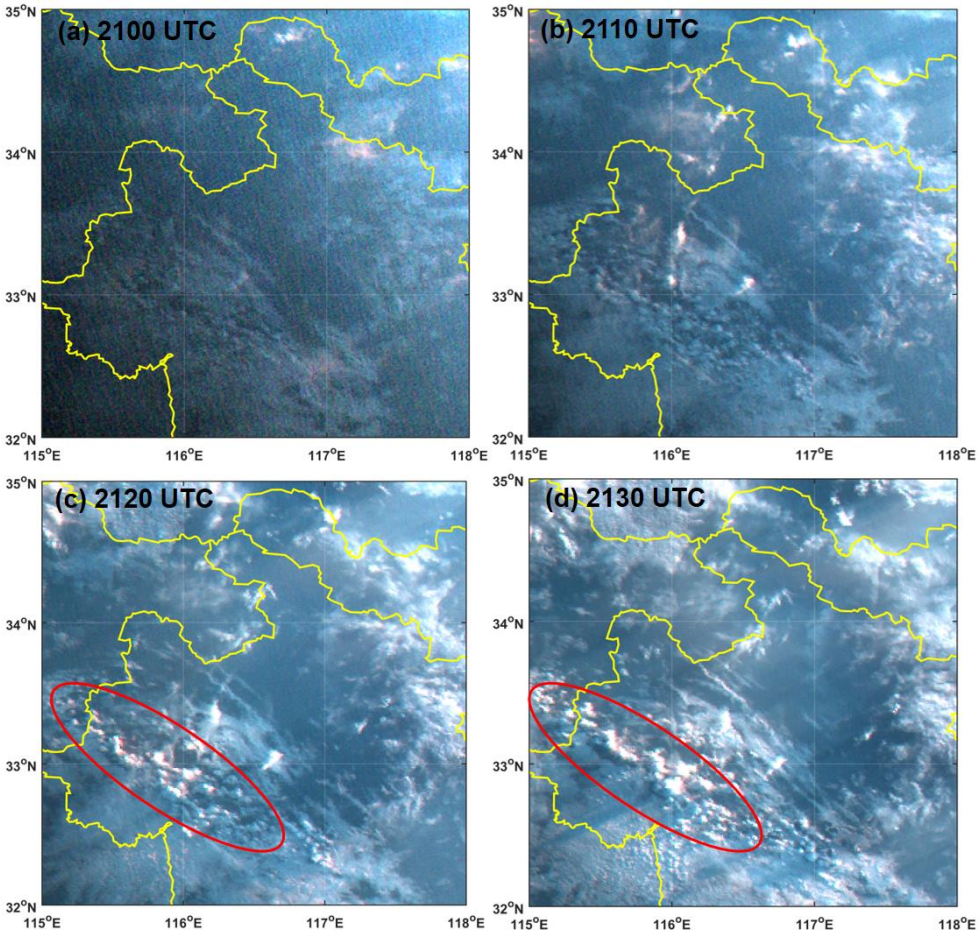

Fig.3 Composite true-color images from Himawari-8 at (a) 2100 UTC, (b) 2110 UTC, (c) 2120 UTC and (d) 2130 UTC 22 June. The linear-organized cumulus cloud cells are circled in red in (c) and (d).

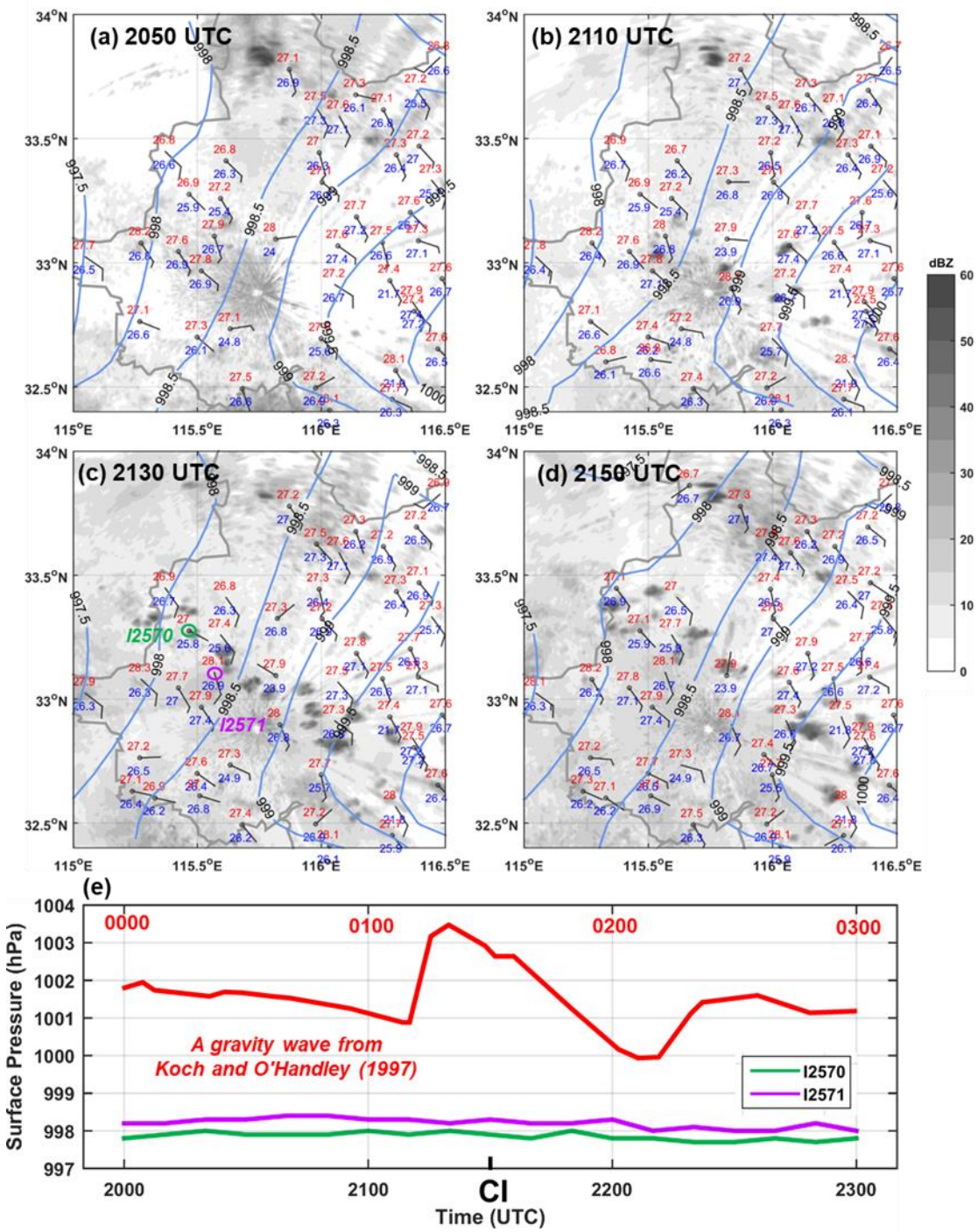

Fig.4 Surface pressure (contoured in blue every 0.5 hPa), surface wind vector (barb=2 m s^{-1}, half barb=1 m s^{-1}), surface temperature (text in red) and surface dewpoint temperature (text in blue) at (a) 2050 UTC, (b) 2110 UTC, (c) 2130 UTC, and (d) 2150 UTC 22 June. The shading denotes the composite reflectivity from the Fuyang radar (dBZ). Time series of surface pressure at station I2570 (green) and I2571 (purple) with locations given in (c) are shown in (e) with CI timing marked on the lower time axis. The pressure trace of a gravity wave from Koch and O'Handley (1997) adapted from their Fig. 18e is also shown in (e) in red with corresponding time (UTC) shown on the upper time axis for reference.

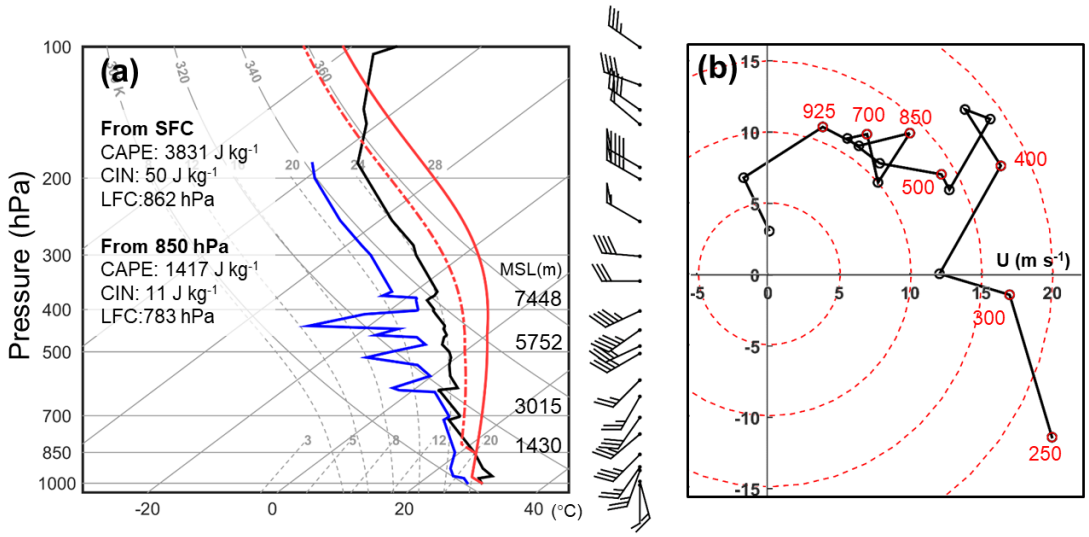

Fig. 5 Skew T–log p (a) and hodograph (b) diagrams of the Fuyang radiosonde (the red cross in Fig. 2d) at 0000 UTC 23 June 2016. (a) The ambient temperature and dewpoint are represented by the solid black and blue lines, respectively; parcels that ascend undiluted from the surface and 850 hPa are shown by the solid and dashed red lines, respectively; the wind profile is shown on the right side (barb=4 m s^{-1}, half barb=2 m s^{-1}, flag=20 m s^{-1}). (b) The velocities at certain pressure levels (hPa) are marked in red circles in the hodograph. CAPE, CIN and LFC of parcels lifted from different levels are given on the left in (a).

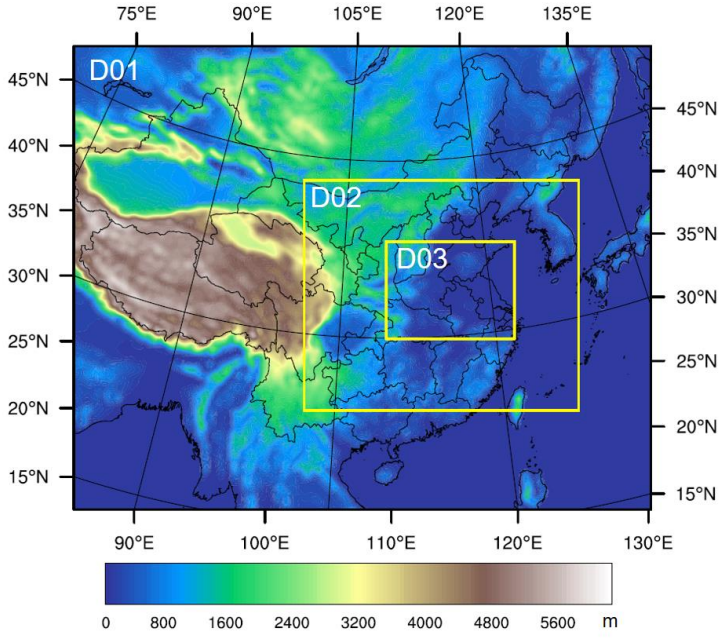

Fig.6 Terrain height (shaded; unit: m) and domains used for the control simulation as well as ensemble forecasts.

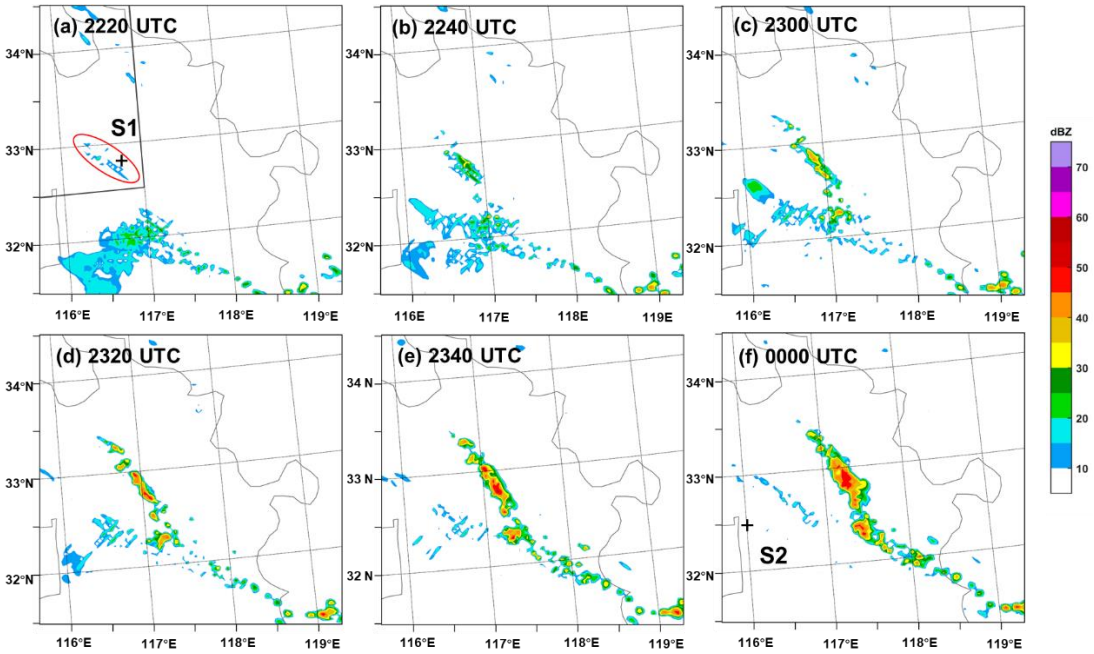

Fig.7 Model-derived composite radar reflectivity (shaded in dBZ) in domain 3 (horizontal resolution of 3 km) of the control simulation at (a) 2220 UTC, (b) 2240 UTC, (c) 2300 UTC, (d) 2320 UTC, and (e) 2340 UTC 22 June and (f) 0000 UTC 23 June. The simulated results hereafter are all from domain 3 (horizontal resolution of 3 km). The weak echo discussed in the text is circled in red in (a). Black crosses in (a) and (f) indicate locations of sounding profiles analyzed in Fig. 8. The area of radar observation in Fig. 2a is given as the gray box in (a).

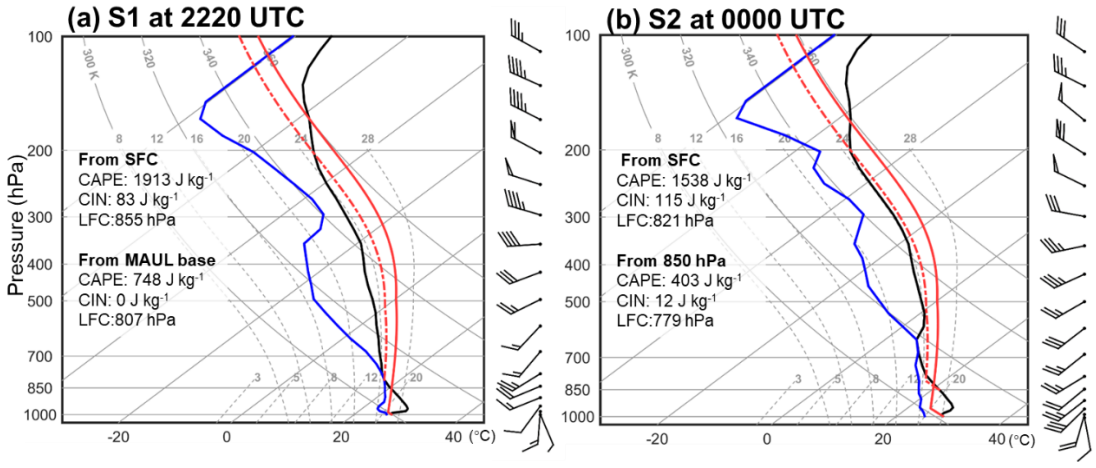

Fig. 8 Skew T–log p diagrams of sounding derived from the control simulation at (a) 2220 UTC 22 June at S1 (black cross in Fig. 7a) and (b) 0000 UTC 23 June at S2 (black cross in Fig.7f). The ambient temperature and dewpoint are represented by the solid black and blue lines, respectively. In (a) S1, parcels that ascend undiluted from the surface and the base of MAUL are shown by the solid and dashed red lines, respectively; In (b) S2, parcels that ascend undiluted from the surface and 850 hPa are shown by the solid and dashed red lines, respectively. The wind profile is shown on the right side (barb=4 m s^{-1}, half barb=2 m s^{-1}, flag=20 m s^{-1}). CAPE, CIN and LFC of parcels lifted from different levels are given on the left.

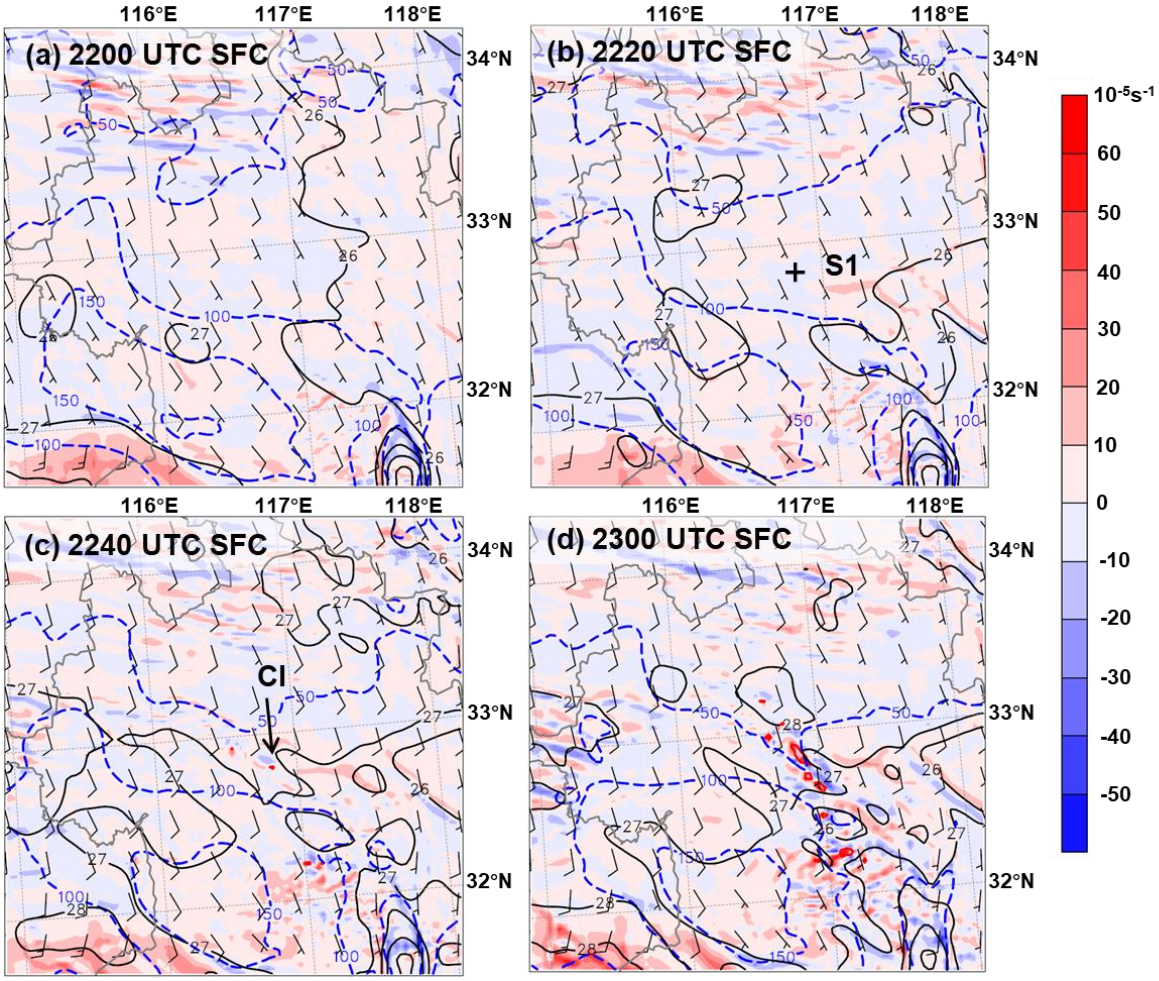

Fig.9 Divergence (shaded every 10^{-5} s^{-1}; blue for convergence and red for divergence), CIN (contoured in dashed blue every 50 J kg^{-1}) and horizontal wind vector (barb=5 m s^{-1}, half barb=2.5 m s^{-1}) at the bottom model level, surface temperature (contoured in solid black every 1°C) and 35-dBZ contour of composite radar reflectivity (solid red) in the control simulation at (a) 2200 UTC, (b) 2220 UTC, (c) 2240 UTC and (d) 2300 UTC 22 June. The first convective cell reaching 35 dBZ is denoted in (c) as CI. The location of S1 given in (b) is the same as in Fig. 7a.

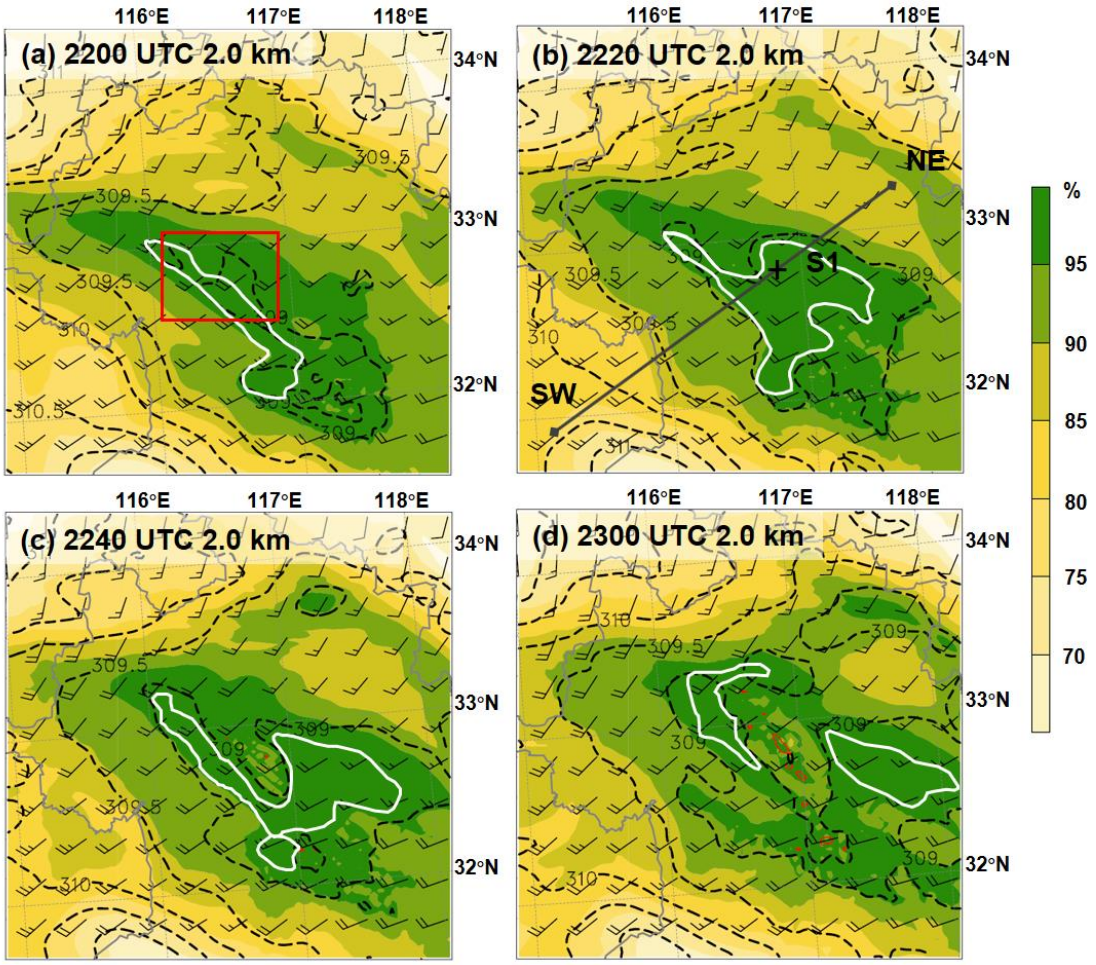

Fig.10 Relative humidity (shaded every 5%), 0.5 J kg^{-1} CIN (contoured in white), horizontal wind vector (barb=5 m s^{-1}, half barb=2.5 m s^{-1}) and potential temperature (contoured in dash black every 0.5 K) at 2.0 km AGL and the 35-dBZ contour (solid red) of composite radar reflectivity (solid red) in the control simulation at (a) 2200 UTC, (b) 2220 UTC, (c) 2240 UTC and (d) 2300 UTC 22 June. The location of S1 is the same as in Fig. 7a, and the cross section in Fig. 11a and Fig. 13 is given in (b). The red box denotes the area used for diagnosing the area-averaged transport of water vapor mixing ratio and potential temperature in Fig. 14.

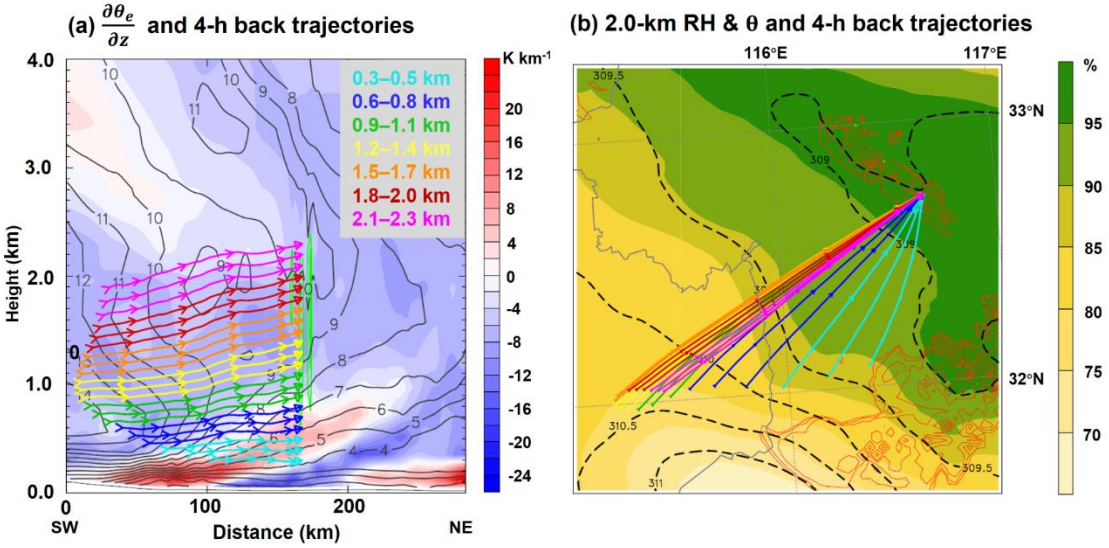

Fig.11 (a) Vertical distributions of 4-h back trajectories of parcels released from the 10-dBZ radar echo at 2220 UTC 22 June with different heights (0.3–2.3 km AGL; colors correspond to different heights as shown in the top-right box) along the plane of the cross section in Fig. 10b; also shown are potential instability ($\partial\theta_e/\partial z$, shaded every 2 K km^{-1}), model-derived composite radar reflectivity (contoured in green at 5-dBZ intervals), and horizontal wind speed along the plane of the cross section (contoured in solid black every 1 m s^{-1}) at 2220 UTC 22 June. (b) Horizontal distributions of the same parcel trajectories as in (a); also shown are relative humidity (shaded at 5% intervals), model-derived radar reflectivity (contoured in red at 5-dBZ intervals) and potential temperature (contoured in black dashes every 0.5 K) at 2.0 km AGL at 2220 UTC 22 June.

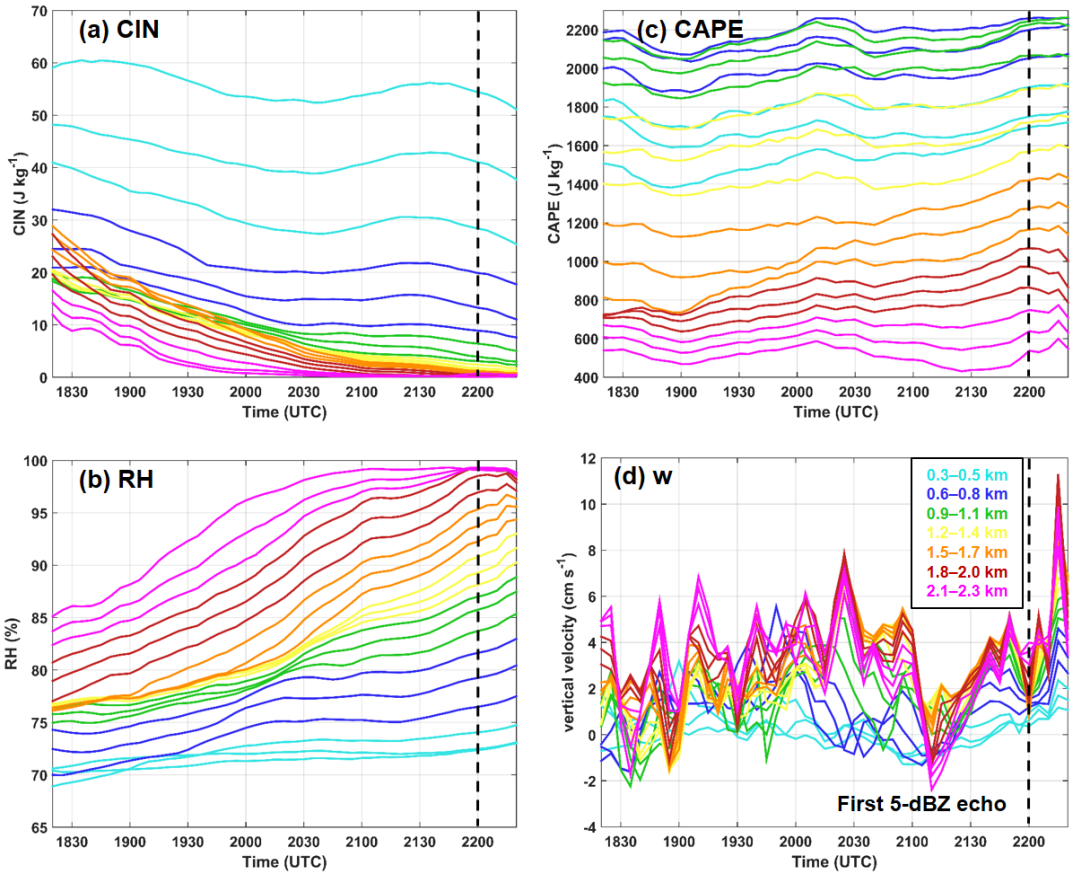

Fig.12 (a) CIN (J kg^{-1}), (b) relative humidity (%), (c) CAPE (J kg^{-1}) and (d) vertical velocity (cm s^{-1}) along the color-coded trajectories plotted in Fig. 11a. The black dashed line indicates the time (2200 UTC 22 June) when the first 5-dBZ echo appeared.

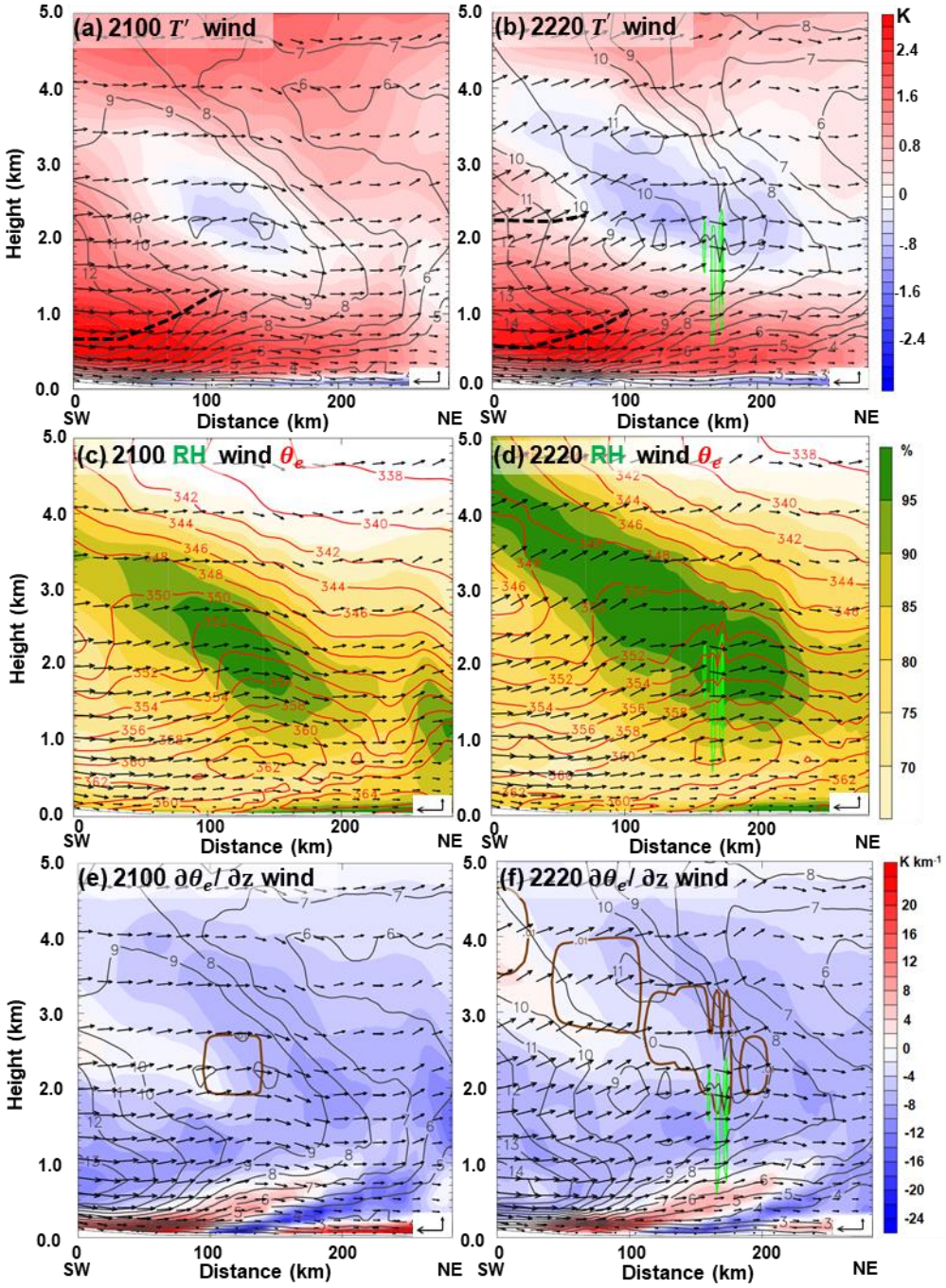

Fig.13 Vertical cross sections along the SW–NE transect in Fig. 10b of temperature perturbation (shaded at 0.2-K intervals), model-derived radar reflectivity (contoured in green at 5-dBZ intervals), horizontal wind speed along the plane of the cross section (contoured in solid black every 1 m s^{-1}) and circulation vectors in the plane of the cross section at (a) 2100 UTC and (b) 2220 UTC 22 June; the reference state used to compute the temperature perturbation has the same lapse rate (0.0065 K m^{-1} below 11 km) as the U.S. Standard Atmosphere and a sea-level temperature of 301 K from this current case. The second row shows the relative humidity (shaded at 5% intervals), model-derived radar reflectivity (contoured in green at 5-dBZ intervals), equivalent

potential temperature (contoured in red every 2 K) and circulation vectors in the plane of the cross section at (c) 2100 UTC and (d) 2220 UTC 22 June. The third row shows the potential instability ($\partial\theta_e/\partial z$, shaded every 2 K km^{-1}), model-derived radar reflectivity (contoured in green at 5-dBZ intervals), cloud water mixing ratio (0.01 g kg^{-1} contour in solid brown), horizontal wind speed along the plane of the cross section (contoured in solid black every 1 m s^{-1}) and circulation vectors in the plane of the cross section at (e) 2100 UTC and (f) 2220 UTC 22 June. The reference vector is given at the bottom right and denotes a horizontal velocity of 10 m s^{-1} and a vertical velocity of 10 cm s^{-1}. The jet axes of the LLJ mentioned in the text are qualitatively denoted by the bold black dashed lines in (a) and (b).

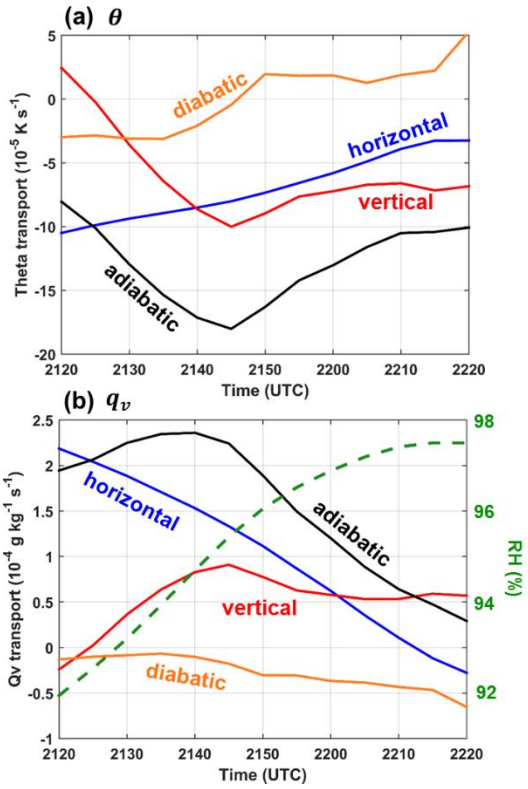

Fig. 14 (a) Evolution of the area-averaged horizontal advection ($-\boldsymbol{V}\cdot\nabla_h\theta$, solid blue), vertical transport ($-w\frac{\partial\theta}{\partial z}$, solid red), diabatic term (D_θ, solid orange) and adiabatic term ($-\boldsymbol{V}\cdot\nabla_h\theta - w\frac{\partial\theta}{\partial z}$, solid black) of potential temperature within the subsequent MAUL (unit: 10^{-5} K s^{-1}) on 22 June. (b) is similar to (a) except for the water vapor mixing ratio (unit: 10^{-4} g kg^{-1} s^{-1}). The evolution of the area-averaged relative humidity within the subsequent MAUL is also plotted as the dashed green line in (b). The area used for averaging is denoted as the red box in Fig. 10a.

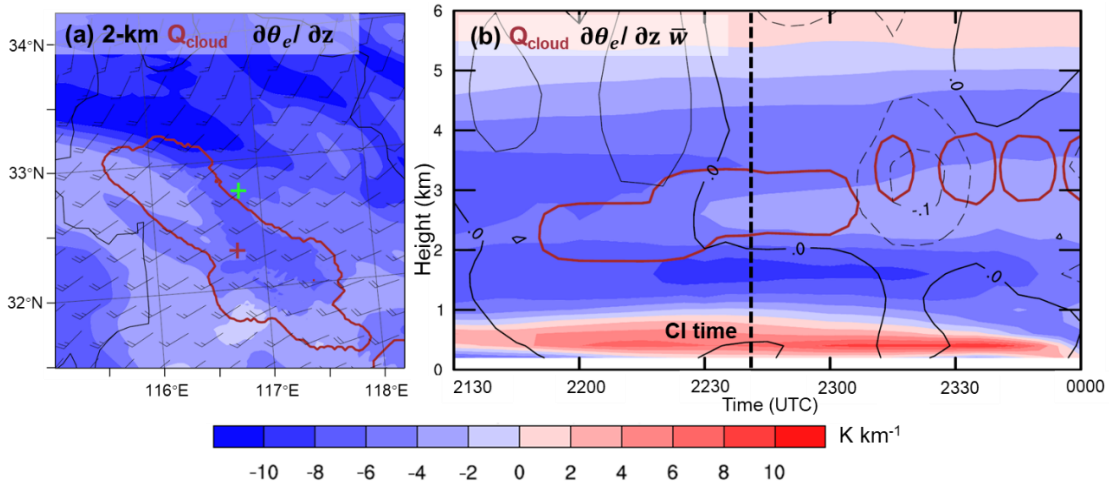

Fig.15 Temporal and spatial scale of the simulated MAUL. (a) Potential instability ($\partial\theta_e/\partial z$, shaded every 2 K km^{-1}), cloud water mixing ratio (0.01 g kg^{-1} contour in solid brown) and horizontal wind vector (barb=5 m s^{-1}, half barb=2.5 m s^{-1}) at 2 km AGL at 2200 UTC 22 June. The CI location (first 35-dBZ echo at 2240 UTC 22 June) is denoted by the green cross. (b) Time series of vertical conditions at the grid point denoted by the brown cross in (a), potential instability ($\partial\theta_e/\partial z$, shaded every 2 K km^{-1}), cloud water mixing ratio (0.01 g kg^{-1} contour in solid brown) and 20-min-averaged vertical velocity (contoured in solid black for positive and negative in black dashes every 0.05 m s^{-1}). The CI timing (2240 UTC 22 June) is marked in black dashes in (b).

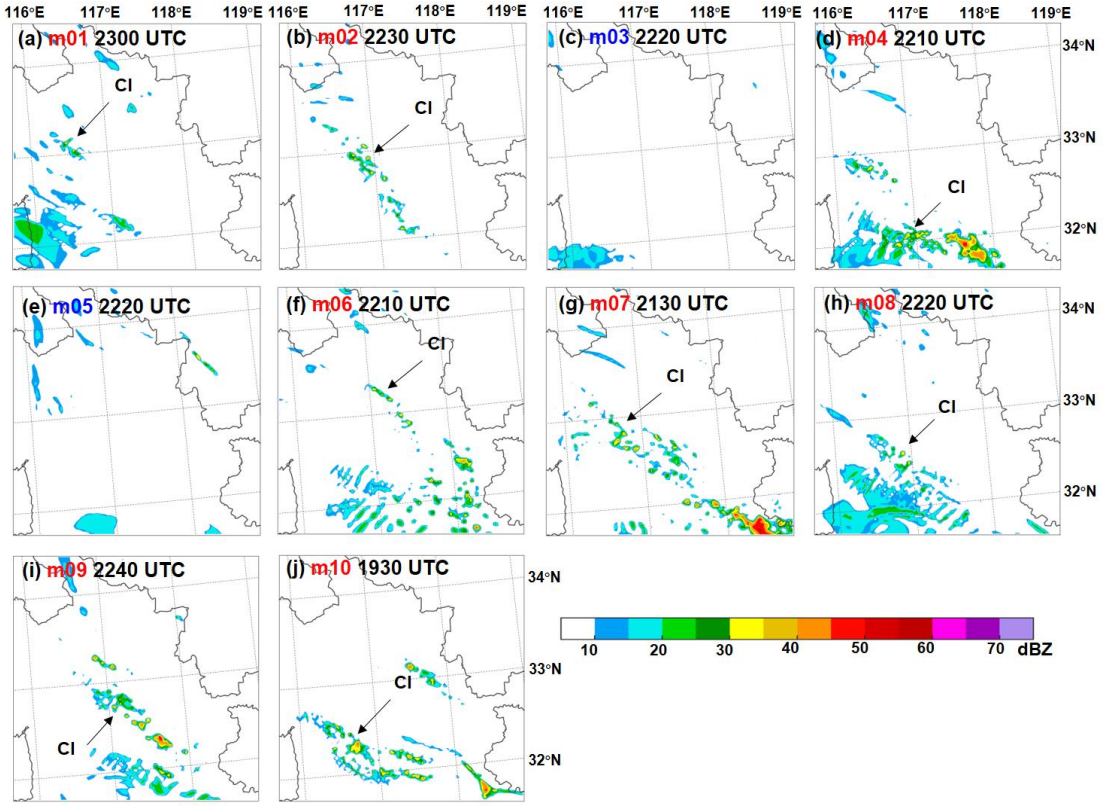

Fig.16 Model-derived (d03) composite radar reflectivity (shaded in dBZ) of the 10 ensemble members (a)–(j). CI members (red label) are plotted at respective CI timing, and non-CI members (blue label) are plotted at 2220 UTC 22 June for comparison.

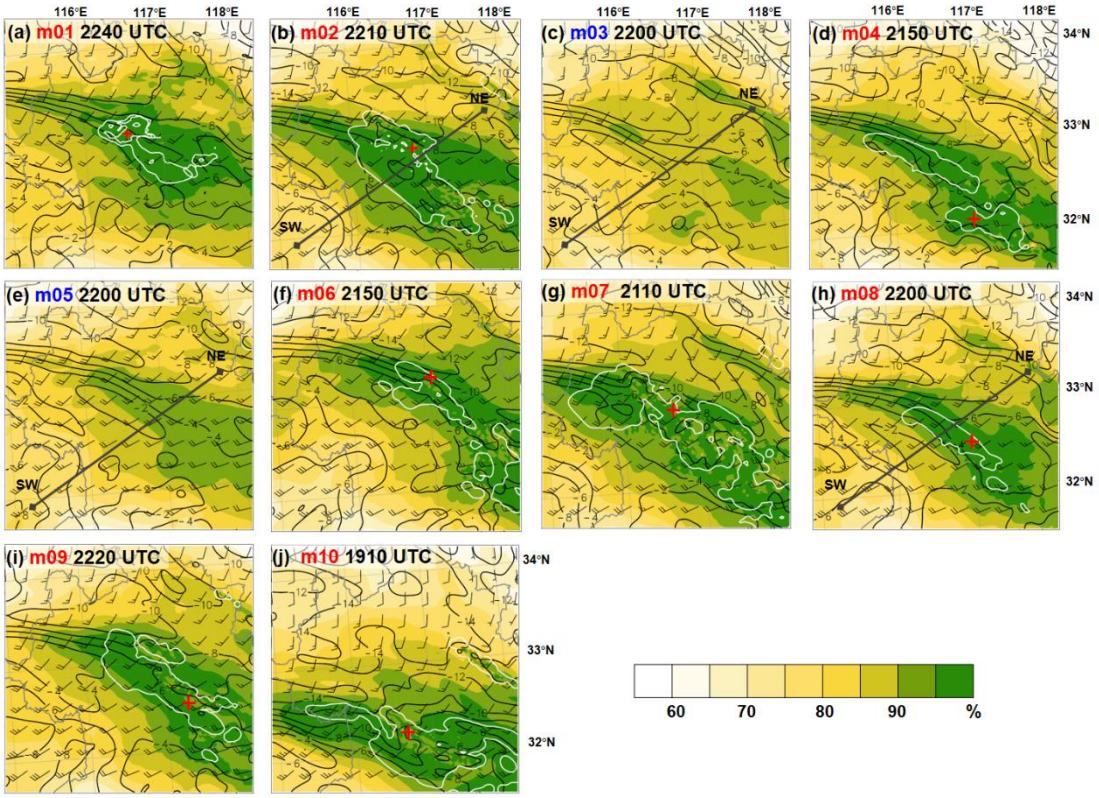

Fig. 17 Distribution of elevated saturated area 20 min before CI including relative humidity (shaded every 5%), horizontal wind vector (barb=5 m s^{-1}, half barb=2.5 m s^{-1}), potential instability ($\partial\theta e/\partial z$, contoured in solid black every 2 K km^{-1}) and cloud water mixing ratio (solid white, contours of 0.01 g kg^{-1}) at 2.0 km AGL in 10 ensemble members (a)–(j). The solid black lines in (b), (c), (e) and (h) indicate the SW–NE path of the cross section in Fig. 18. The CI locations shown in Fig. 16 are marked as red crosses.

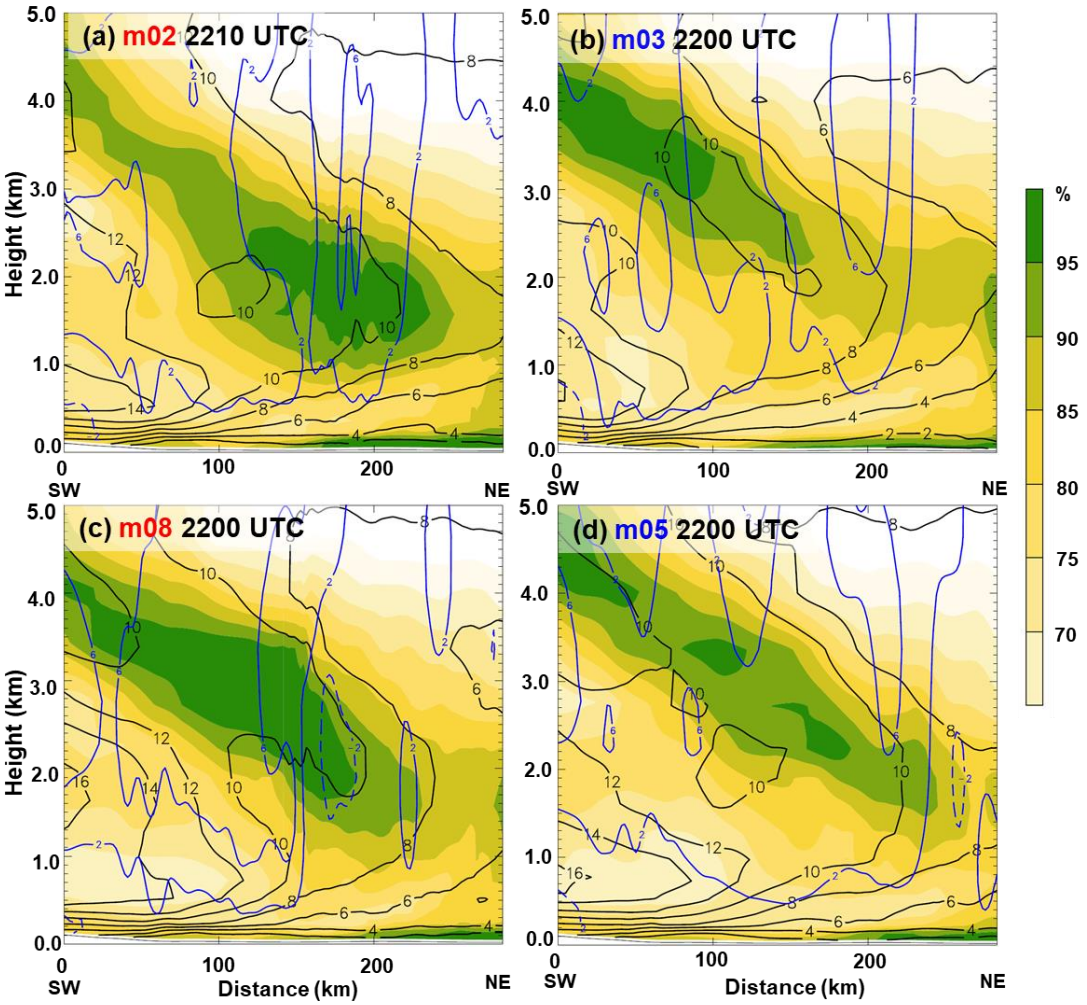

Fig. 18 Vertical cross sections along the SW–NE transect of typical CI and non-CI members in Fig. 17b, c, e and h, including relative humidity (shaded every 5%), horizontal wind speed along the plane of the cross section (contoured in solid black every 2 m s^{-1}), and 20-min-averaged vertical velocity (contoured in blue with positive (> 2 cm s^{-1}) in solid lines and negative (< −2 cm s^{-1}) in dashes every 4 cm s^{-1}) in (a) member 02 at 2210 UTC 22 June, (b) member 03 at 2200 UTC 22 June, (c) member 08 at 2200 UTC 22 June and (d) member 05 at 2200 UTC 22 June.